



**HAL**  
open science

## Two-dimensional model for the martian exosphere: Applications to hydrogen and deuterium Lyman $\alpha$ observations

D. Bhattacharyya, Jean-Yves Chaufray, M. Mayyasi, J.T. Clarke, S. Stone,  
R.V. Yelle, W. Pryor, Jean-Loup Bertaux, Justin Deighan, S.K. Jain, et al.

► **To cite this version:**

D. Bhattacharyya, Jean-Yves Chaufray, M. Mayyasi, J.T. Clarke, S. Stone, et al.. Two-dimensional model for the martian exosphere: Applications to hydrogen and deuterium Lyman  $\alpha$  observations. *Icarus*, 2020, 339 (15 March), pp.art. 113573. 10.1016/j.icarus.2019.113573 . insu-02397197

**HAL Id: insu-02397197**

**<https://insu.hal.science/insu-02397197>**

Submitted on 16 Dec 2020

**HAL** is a multi-disciplinary open access archive for the deposit and dissemination of scientific research documents, whether they are published or not. The documents may come from teaching and research institutions in France or abroad, or from public or private research centers.

L'archive ouverte pluridisciplinaire **HAL**, est destinée au dépôt et à la diffusion de documents scientifiques de niveau recherche, publiés ou non, émanant des établissements d'enseignement et de recherche français ou étrangers, des laboratoires publics ou privés.

1 **Two-Dimensional Model for the Martian Exosphere: Applications to**  
2 **Hydrogen and Deuterium Lyman  $\alpha$  Observations**

3  
4 D. Bhattacharyya<sup>1</sup>, J. Y. Chaufray<sup>2</sup>, M. Mayyasi<sup>1</sup>, J. T. Clarke<sup>1</sup>, S. Stone<sup>3</sup>, R. V. Yelle<sup>3</sup>, W.  
5 Pryor<sup>4</sup>, J. L. Bertaux<sup>2</sup>, J. Deighan<sup>5</sup>, S. K. Jain<sup>5</sup>, and N. M. Schneider<sup>5</sup>

6  
7 1. *Center for Space Physics, Boston University, 725 Commonwealth Avenue, Boston MA*  
8 *02215, USA*

9 2. *LATMOS/CNRS, 78280 Guyancourt, France*

10 3. *Lunar and Planetary Laboratory, University of Arizona, 1629 E University Blvd., Tucson*  
11 *AZ 80092, USA*

12 4. *Science Division, Central Arizona College, Coolidge, AZ 85128, USA*

13 5. *Laboratory of Atmospheric and Space Physics, Boulder, CO 80303, USA*

14  
15  
16  
17  
18 To be submitted to *Icarus*

19  
20  
21 43 Pages

22 1 Table

23 7 Figures

31 **Proposed running title:** 2-D radiative transfer model for Mars

32

33 **Corresponding author address:**

34 Dolon Bhattacharyya

35 Center for Space Physics

36 Boston University

37 725 Commonwealth Avenue

38 Boston MA 02215, USA

39 e-mail: [dolonb@bu.edu](mailto:dolonb@bu.edu)

40

41

42

43

44

45

46

47

48

49

50

51

52

53

54

55

56

57

58

59

60

61

62 **Abstract**

63 The analysis of Lyman  $\alpha$  observations in the exosphere of Mars has become limited by the  
64 assumption of spherical symmetry in the modeling process, as the models are being used to analyze  
65 increasingly detailed measurements. In order to overcome this limitation, a two-dimensional  
66 density model is presented, which better emulates the density distribution of deuterium and  
67 hydrogen atoms in the exosphere of Mars. A two-dimensional radiative transfer model developed  
68 in order to simulate multiple scattering of solar Lyman  $\alpha$  photons by an asymmetric, non-  
69 isothermal hydrogen exosphere, is also presented here. The models incorporate changes in density  
70 and temperature structure of the martian atmosphere with radial distance and solar zenith angle.  
71 The 2-D models were applied to the MAVEN-IUVS echelle observations of deuterium and  
72 hydrogen Lyman  $\alpha$  as well as HST Lyman  $\alpha$  observations of hydrogen at Mars. The asymmetric  
73 2-D model provided better fits to the data and smaller thermal escape rates in comparison to the  
74 symmetric 1-D model for the exosphere of Mars. However, intensity differences between both  
75 models became small above  $\sim 2.5$  martian radii indicating that the exosphere of Mars approaches  
76 spherical symmetry at higher altitudes, in agreement with earlier studies. In addition, a new cross  
77 calibration of the absolute sensitivities of two instruments on the Hubble Space Telescope and the  
78 MAVEN-IUVS echelle mode is presented based on near-simultaneous observations of the  
79 geocorona and Mars.

80

81

82

83

84

85

86

87

88

89

90

91

92 **Keywords:** Mars; Atmosphere; Ultraviolet observations; Radiative transfer

93 **1. Introduction**

94 Resonantly scattered solar Lyman  $\alpha$  photons by martian exospheric hydrogen have been studied  
95 for decades before the transition into 21<sup>st</sup> century [Barth et al., 1969, 1971; Anderson and Hord,  
96 1971, 1972; Babichenko et al., 1976; Dostovalov and Chuvakhin, 1973]. This Lyman  $\alpha$  emission  
97 at 1215.67 Å was observed to extend to very high altitudes, beyond 30,000 km ( $\sim 8.8 R_{\text{Mars}}$ ) [Barth  
98 et al., 1969]. Photochemical modeling indicated that most of the exospheric H atoms originated  
99 from the photo-dissociation of water vapor by ultraviolet sunlight close to the planet's surface  
100 [Hunten and McElroy, 1970; McElroy and Donahue, 1972; Parkinson and Hunten, 1972]. This  
101 realization piqued an interest towards understanding the properties of martian exospheric hydrogen  
102 as it could provide an insight into the disappearance of Mars' water. Since the majority of H atoms  
103 at Mars were theorized to be escaping by the thermal mechanism of Jeans escape [Hunten, 1973,  
104 1982], knowledge about the density distribution and the temperature of the H atoms was deemed  
105 necessary to constrain the present-day escape rate of H/H<sub>2</sub>O from Mars.

106 Observations of the martian Lyman  $\alpha$  emission conducted in the past decade revealed  
107 significant seasonal changes in H escape rate, with the peak escape occurring close to Mars'  
108 southern summer solstice ( $L_s = 270^\circ$ ) [Clarke et al., 2014; 2017; Chaffin et al., 2014; Bhattacharyya  
109 et al., 2015; 2017b; Romanelli et al., 2016; Halekas et al., 2017; Rahmati et al., 2017; 2018]. These  
110 large seasonal changes were not expected from earlier photochemical modeling of the martian  
111 atmosphere [Hunten 1973; Krasnopolsky 2002], and are believed to be a result of a combination  
112 of atmospheric upwelling and dust storm activity lifting water vapor to higher altitudes around  
113 Mars' perihelion [Chaffin et al., 2017; Fedorova et al., 2017; Heavens et al., 2018; Clarke, 2018].  
114 This discovery has implications for understanding the water escape history of Mars. Analysis of  
115 the observations also revealed the possibility of the presence of an energetic population of  
116 hydrogen along with thermal H in the martian exosphere, which could increase ( $\sim$ factor of 2) the  
117 present-day escape rate of hydrogen from Mars [Chaufray et al., 2008; Bhattacharyya et al.,  
118 2017a]. More recently, an enhancement in martian hydrogen escape was also detected by the  
119 Imaging Ultraviolet Instrument (IUVS) [McClintock et al., 2015] onboard the Mars Atmosphere  
120 Volatile Evolution (MAVEN) spacecraft during a series of strong solar flare events and a coronal  
121 mass ejection that swept past Mars [Mayyasi et al., 2018]. These findings about the martian  
122 exosphere in the past decade indicate that the water escape scenario at Mars is complicated, and

123 all the significant factors that influence hydrogen escape at Mars have to be modeled, analyzed  
124 and studied in detail before an accurate estimate of the timeline of Mars's water loss is made.

125 Lyman  $\alpha$  emission from deuterium at 1215.33 Å, the heavier isotope of hydrogen, on the  
126 other hand, has only recently been studied in detail to determine the D/H ratio at Mars [Clarke et  
127 al., 2017; Mayyasi et al., 2017b; 2019]. The deuterium to hydrogen ratio is a good indicator of a  
128 planet's water loss in the past through atmospheric escape. The lightest gases from every terrestrial  
129 planet in our solar system are slowly evaporating into space. In the case of hydrogen and its heavier  
130 isotope deuterium, hydrogen is escaping much faster than deuterium due to the difference in their  
131 masses. Such an escape imbalance over long periods of time would enhance the D/H ratio in a  
132 planet's atmosphere, thereby providing an estimate of the amount of atmosphere that has escaped  
133 the planet [Bertaux et al., 1993; Krasnopolsky et al., 1998].

134 Global measurements of D/H ratio through observations of HDO and H<sub>2</sub>O in the martian  
135 atmosphere revealed it to be  $6 \pm 3$  times higher than the standard mean ocean water (SMOW) value  
136 ( $1.5576 \times 10^{-4}$ ) [Owen et al., 1988] indicating an extended history of atmospheric escape from  
137 Mars. A more recent measurement of the martian D/H ratio by the Mars Science Laboratory (MSL)  
138 constrained it to be  $3 \pm 0.2 \times$  SMOW [Mahaffy et al., 2015b]. Further measurement of D/H from  
139 observations of H<sub>2</sub>O and HDO indicated large latitudinal variations with enhancements of  $\sim 7$  times  
140 SMOW in certain areas, which lent further support to the earlier conclusion of bulk atmospheric  
141 loss from Mars [Villanueva et al., 2015]. However, all these measurements were confined to the  
142 lower atmosphere (below an altitude of  $\sim 60$  km) and were indirect estimates of the D/H ratio  
143 through HDO and H<sub>2</sub>O observations, with the assumption that HDO and H<sub>2</sub>O are the major sources  
144 of D and H atoms in the martian exosphere. Observations of martian exospheric deuterium Lyman  
145  $\alpha$  emission (1215.33 Å) with the IUVS-echelle instrument onboard MAVEN over two Mars years,  
146 revealed that deuterium exhibits large seasonal variations like hydrogen, with its peak close to  
147 southern summer solstice [Clarke et al., 2017; Mayyasi et al., 2017b; 2019]. This might result in a  
148 different D/H ratio for the upper atmosphere. Therefore, it is imperative to combine the deuterium  
149 and hydrogen observations with MAVEN and the Hubble Space Telescope (HST) taken in the past  
150 decade and use the most advanced modeling techniques in order to obtain the martian exospheric  
151 D/H value so as to put accurate constraints on the water and atmospheric loss incurred by Mars  
152 over its 4.5-billion-year existence.

153           The MAVEN spacecraft has been in orbit around Mars from September 2014. Since then  
154 its various suite of instruments has been studying the martian atmosphere. Images of the Lyman  $\alpha$   
155 emission from hydrogen in the martian exosphere have revealed it to be spherically asymmetric in  
156 structure [Chaffin et al., 2015]. Similar findings were made with HST [Bhattacharyya et al., 2017a]  
157 and Mars Express (MEX) [Holmström, 2006] which found the hydrogen exosphere at Mars to be  
158 spherically asymmetric below 2.5 martian radii (~8500 km). The Neutral Gas and Ion Mass  
159 Spectrometer (NGIMS) [Mahaffy et al., 2015a] onboard MAVEN has measured atmospheric  
160 temperature differences of > 100 K between the day and the night side of Mars [Stone et al., 2018].  
161 The MAVEN spacecraft, which had an apoapse of ~6000 km and periapse of ~150 km up until  
162 early 2019, conducted observations of martian D and H Lyman  $\alpha$  emissions in a region where the  
163 exospheric structure is not spherically symmetric. Therefore, earlier models which assumed a  
164 spherically symmetric, isothermal exosphere [Anderson and Hord, 1971; Anderson 1974;  
165 Chaufray et al., 2008; Chaffin et al., 2014; 2015; 2018; Bhattacharyya et al., 2015; 2017a; 2017b],  
166 might not accurately capture the actual physical properties of the H and D atoms at Mars.

167           The large difference in exospheric temperature between day and night at Mars, as observed  
168 by MAVEN-NGIMS could affect the model-derived Jeans escape rate of hydrogen when assuming  
169 a spherically symmetric atmosphere. For example, a 250 K exobase temperature and  $10^4 \text{ cm}^{-3}$   
170 density for a symmetric exospheric would result in a Jeans escape rate of  $2.01 \times 10^{25}$  particles/sec  
171 for H, which is ~1.86 times higher than the Jeans escape rate from an asymmetric non-isothermal  
172 atmosphere, in which the temperature trend follows the NGIMS observations (section 2.1) and the  
173 density trend follows the Hodges and Johnson [1968] formulation for light species (section 2.2).  
174 Therefore, in this paper, a more physically accurate two-dimensional model of the martian  
175 exosphere is presented which is being applied to study the H and D Lyman  $\alpha$  emissions from  
176 MAVEN and HST in order to provide better constraints on the H escape rates at Mars, which in  
177 turn, would help estimate the actual amount of water lost by Mars.

178           Section 2 summarizes the two-dimensional atmosphere model for a non-symmetric, non-  
179 isothermal atmosphere unlike the standard Chamberlain model [Chamberlain, 1963] usually used  
180 to derive exospheric density distributions of the lightest atomic species for terrestrial planets.  
181 Section 3 summarizes the two-dimensional radiative transfer model which accounts for a non-  
182 spherical, non-isothermal atmosphere in order to simulate the optically thick H Lyman  $\alpha$  emission  
183 at Mars. Section 4 presents the application of the asymmetric model to MAVEN and HST

184 observations as well as comparisons between the symmetric and asymmetric model to MAVEN  
185 observations of D and H Lyman  $\alpha$  emissions and HST observations of H Lyman  $\alpha$  emission.  
186 Section 5 presents a discussion and summary of the results and implications of this work towards  
187 characterizing the martian exosphere. Appendix A and B details the 2-D atmosphere model as well  
188 as the non-spherical, non-isothermal radiative transfer model developed for the analysis of the  
189 MAVEN and HST observations.

190

## 191 **2. Two-Dimensional density model of the martian exosphere**

192 It was expected, and MEX, HST, and MAVEN data have confirmed, that the martian upper  
193 atmosphere is highly asymmetric in density and temperature [Holmström, 2006; Bhattacharyya et  
194 al., 2017a; Chaffin et al., 2015; Stone et al., 2018]. This asymmetric nature of the martian  
195 exosphere necessitates the usage of models which accounts for a non-symmetric, non-isothermal  
196 exosphere while analyzing the data from various instruments. In the modeling process, the exobase  
197 density and temperature are varied in the radial direction and with solar zenith angle (SZA) to  
198 simulate the martian exosphere. While in the future a more complex local time dependence may  
199 be considered in the modeling process, here variation of atmospheric characteristics with only solar  
200 zenith angle is considered in an effort to improve the models, as SZA variation is a significant one  
201 recorded in the MAVEN data [Stone et al., 2018].

202 The 2-dimensional density model assumes that the arbitrary altitude at which the atmosphere  
203 transitions from the collisional to collisionless regime (exobase altitude) to be 200 km at Mars.  
204 The model atmosphere has an upper boundary at 50,000 km and a lower boundary at 80 km. Lyman  
205  $\alpha$  is completely absorbed by CO<sub>2</sub> at Mars at altitudes below 80 km. Thus, the region below 80 km  
206 is opaque at this UV wavelength, which is why the altitude of 80 km is taken as the lower  
207 atmospheric boundary in the modeling process.

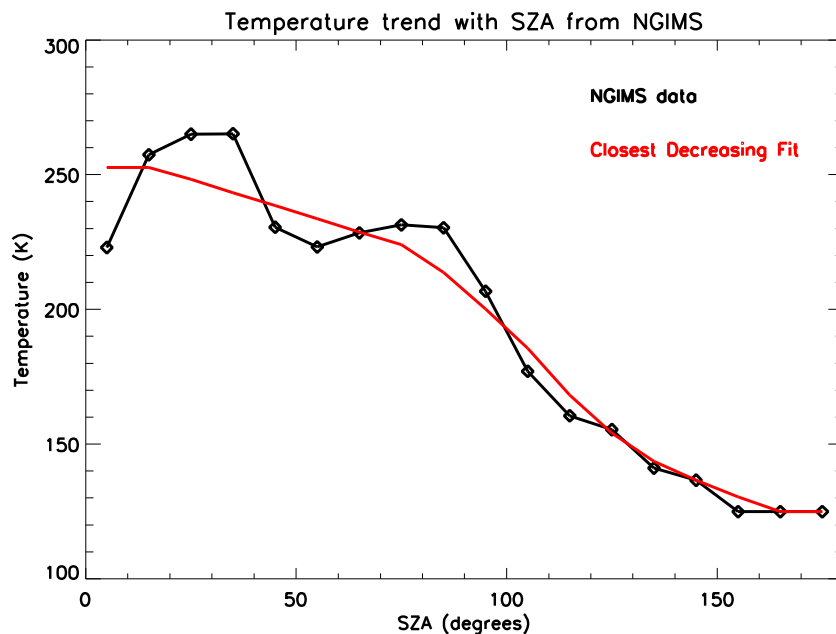
208 The 2-D model has only one free parameter, the exobase density of either thermal D or H at  
209 SZA = 0°. The exobase temperature for thermal H/D is pre-determined from existing alternate  
210 observations of other neutral species like CO<sub>2</sub> and Ar present in the martian atmosphere. This is  
211 necessary as there exists degeneracy between the temperature and density parameters when  
212 analyzing optically thick emissions like Lyman  $\alpha$  [Bhattacharyya et al., 2017]. Therefore, the  
213 accuracy of modeling results is highly dependent on a correct representation of the temperature



214 structure for the martian atmosphere which necessitated the development of a 2-D model in light  
215 of the MAVEN-NGIMS derived temperature differences between the day and night side of Mars.  
216

217 *2.1 Variation of temperature with SZA, solar longitude, and altitude*

218 MAVEN observations of the martian atmosphere made over the course of approximately two Mars  
219 years by the NGIMS instrument were used to determine the variation of Mars' exospheric  
220 temperature with SZA [Stone et al., 2018]. Figure 1 shows this trend as observed by MAVEN. The  
221 black line represents the data averaged over a large number of measurements and the red line is  
222 the closest decreasing fit to the data. The small variations in the data is most likely the result of  
223 MAVEN's constantly changing viewing geometry combined with changes in solar activity over  
224 the two Mars years. The closest decreasing fit eliminates these variations in the data by assuming  
225 that the temperature can only decrease with SZA. This delivers a dayside trend agreeable with  
226 Mars Global Circulation Models (MGCM) [Bougher et al., 2015; Chaufray et al., 2018]. Given a  
227 temperature at SZA = 0°, the curve depicted by the red line is then used to determine the variation  
228 of temperature with SZA. Figure 1 below, which is an adaptation of figure 2 from Mayyasi et al.,  
229 [2019], has been included in this paper in order to present a more robust discussion of the models  
230 which make extensive use of this temperature trend.



231

232 **Figure 1:** *Exobase temperature trend with solar zenith angle determined from analysis of NGIMS*  
 233 *observations of the martian atmosphere. The black line depicts measurements made by MAVEN –*  
 234 *NGIMS whereas the red line is the closest decreasing fit to the data.*

235 The exobase temperature at  $SZA = 0^\circ$  for thermal H and D at Mars for a particular solar  
 236 longitude ( $L_s$ ) along Mars' orbit is pre-determined by fitting the MAVEN-NGIMS derived  
 237 temperatures for the lower thermosphere at perihelion and aphelion with a sine wave given by

$$238 \quad y(L_s) = A \sin\left(\frac{(L_s - 1.239)}{2} \text{ radians}\right) + B \quad (1)$$

239 In the above equation  $y$  represents the temperature at  $SZA = 0^\circ$  for a particular  $L_s$ ,  $A$  is the  
 240 difference between the aphelion and perihelion derived NGIMS temperatures at  $SZA = 0^\circ$  and  $B$   
 241 is the aphelion temperature at  $SZA = 0^\circ$ . NGIMS observations at aphelion and perihelion included  
 242 a large sample of measurements covering solar zenith angles from  $\sim 50^\circ$  to  $110^\circ$  at aphelion and  
 243  $\sim 5^\circ - 140^\circ$  at perihelion. This data was used to constrain the exobase temperature at  $SZA = 0^\circ$  by  
 244 extrapolating the temperature curve of Figure 1 as well as shifting it up/down to match the derived  
 245 temperatures at their corresponding solar zenith angles for aphelion and perihelion.

246 Mars' thermospheric temperatures at aphelion and perihelion were determined using NGIMS  
 247 observations of  $CO_2$  and Ar densities at MAVEN's periapsis altitudes ( $\sim 150$ - $180$  km). The slope  
 248 of the  $CO_2$  and Ar density measurements between  $160 - 220$  km were used to derive the  
 249 atmospheric scale height, and thereby the temperature of the background atmosphere. Since the  
 250 difference in the derived temperature values from the scale heights of  $CO_2$  and Ar were within the  
 251 measurement uncertainties, the values were averaged to determine the martian thermospheric  
 252 temperature at aphelion and perihelion for the available solar zenith angles. The temperature curve  
 253 represented in Fig. 1 was then utilized to approximate the exobase temperature at the sub-solar  
 254 point [Mayyasi et al., 2019]. The resulting aphelion and perihelion temperatures at the exobase  
 255 altitude of  $200$  km and  $SZA = 0^\circ$  for Mars were determined to be  $216 \pm 39$  K and  $255 \pm 29$  K  
 256 respectively [Mayyasi et al., 2019]. These temperatures are only representative of exospheric  
 257 populations of D and H that are in thermal equilibrium with the bulk atmosphere (i.e.  $CO_2$ ) below  
 258 the exobase. Temperature of non-thermal D and H cannot be estimated using this method.

259 The temperature variations with altitude were determined from the analytical expression of  
 260 Krasnopolsky [2002]. At present this is the only existing analytical expression for determining  
 261 temperature variation with altitude and was established using Viking 1's measurement of neutral  
 262 densities (CO<sub>2</sub>, N<sub>2</sub>, CO, O<sub>2</sub> and NO) at Mars between 120-200 km. This functional form was  
 263 modified to include a SZA dependence and is written as:

$$264 \quad T(z, sza) = T_{\infty}(sza) - (T_{\infty}(sza) - 125)e^{-\frac{(z-90)^2}{11.4T_{\infty}(sza)}} \quad (2)$$

265  $T_{\infty}$  here represents a temperature at a reference altitude of 300 km, and is taken to be slightly higher  
 266 than the pre-determined temperature at the exobase altitude (200 km) such that the temperature  
 267 curve derived using eq. (2) intersects the known exobase temperature value. The variable  $z$  in the  
 268 equation represents an altitude range of 80 – 200 km. Beyond 200 km the temperature assumes the  
 269 value of the exobase temperature for a particular SZA. Figure 2 shows the temperature curves  
 270 derived for a solar longitude of 74° and 251.6° for Mars for a non-isothermal atmosphere.

## 271 *2.2 Variation of Deuterium and Hydrogen density with SZA, solar longitude and altitude*

272 The variation of density with SZA for both D and H is calculated by using the Hodges and Johnson  
 273 [1968] formulation for light species, where the species density at the exobase is determined to be  
 274 a function of only the exobase temperature and is given by the relation,

$$275 \quad n T^{5/2} = \text{constant} \quad (3)$$

276 In the above equation  $n$  represents the exobase density of the species and  $T$  represents the exobase  
 277 temperature of the species at a particular SZA. This relationship holds true for hydrogen because  
 278 H density near the exobase adjusts with local temperature changes such that the net local upward  
 279 ballistic flux is balanced by the net local downward ballistic flux. There is no influx of additional  
 280 H atoms into the exosphere as the ballistic transport timescale is shorter than the vertical diffusion  
 281 timescale of H into the exosphere through the lower atmosphere. This was confirmed through Mars  
 282 Global Circulation Model (MGCM) simulations for hydrogen [Chaufray et al., 2018]. In the  
 283 modeling process presented here, it was assumed that deuterium, the heavier isotope of hydrogen,  
 284 also obeys this relationship.

285 The density profile with altitude for D and H calculated at Mars extends from 80 km to  
 286 50,000 km in the model. The process of constructing the density profile with altitude involves  
 287 three different approaches applied to three different altitude ranges.

288      2.2.1 *Above the exobase: 200 – 50,000 km*

289      The region above the exobase is considered to be almost collisionless. In a 1-D situation, where  
 290      the exosphere is considered to be spherically symmetric and isothermal, the Chamberlain  
 291      approximation [Chamberlain, 1963] works well for different planetary bodies. Chamberlain’s  
 292      theory makes the assumption that the exospheric atoms at the exobase level obey the Maxwell-  
 293      Boltzmann velocity distribution with a single mean temperature, which is the exobase temperature.  
 294      However, in the case of a non-spherically symmetric and non-isothermal atmosphere a classical  
 295      Chamberlain approach is not applicable. In order to simulate exospheric densities for an  
 296      asymmetric atmosphere, the approach developed by Vidal-Madjar and Bertaux [1972] was  
 297      adopted here. Under this approach, the exosphere is considered to be made up of populations of  
 298      particles which obey the Maxwell-Boltzmann velocity distribution with different mean  
 299      temperatures corresponding to different launch points on the exobase. The particle distribution  
 300      function has a Maxwellian form that depends on the velocity ( $V_c$ ), the longitude ( $\alpha_c$ ) and the  
 301      latitude ( $\delta_c$ ) at the critical altitude, i.e. the exobase of Mars and has the form given by:

$$302 \quad f_c(\alpha_c, \delta_c, V_c) = N_c(\alpha_c, \delta_c) \left[ \frac{1}{2\pi m k_b T_c(\alpha_c, \delta_c)} \right]^{3/2} \exp \left[ \frac{-m M G V_c^2}{r_c k_b T_c(\alpha_c, \delta_c)} \right] \quad (4)$$

303      Here  $N_c(\alpha_c, \delta_c)$  is the number density at the exobase as a function of the longitude and latitude,  
 304       $m$  the mass of the species,  $k_b$  the Boltzmann’s constant,  $T_c(\alpha_c, \delta_c)$  the exobase temperature which  
 305      is also a function of longitude and the latitude,  $r_c$  the exobase altitude (200 km for Mars),  $V_c$  the  
 306      velocity at the exobase normalized to the escape velocity,  $M$  the mass of the planet and  $G$  the  
 307      universal gravitational constant. The number density at any point in space is written as:

$$308 \quad N_c(y, \alpha_c, \delta_c) = \int f_c d^3 p_i \quad (5)$$

309      The above integral is over the total population that occupies an element of momentum space ( $d^3 p_i$ )  
 310      and is restricted to existing trajectories of particles (ballistic, satellite and escaping trajectories)  
 311      that may occupy the momentum space. The subscript  $i$  represents the  $i^{\text{th}}$  particle ( $i = 1, 2, \dots, n$ ).  
 312      Satellite trajectories are neglected in the model. Appendix A details the Vidal-Madjar and Bertaux  
 313      [1972] approach used in this study.

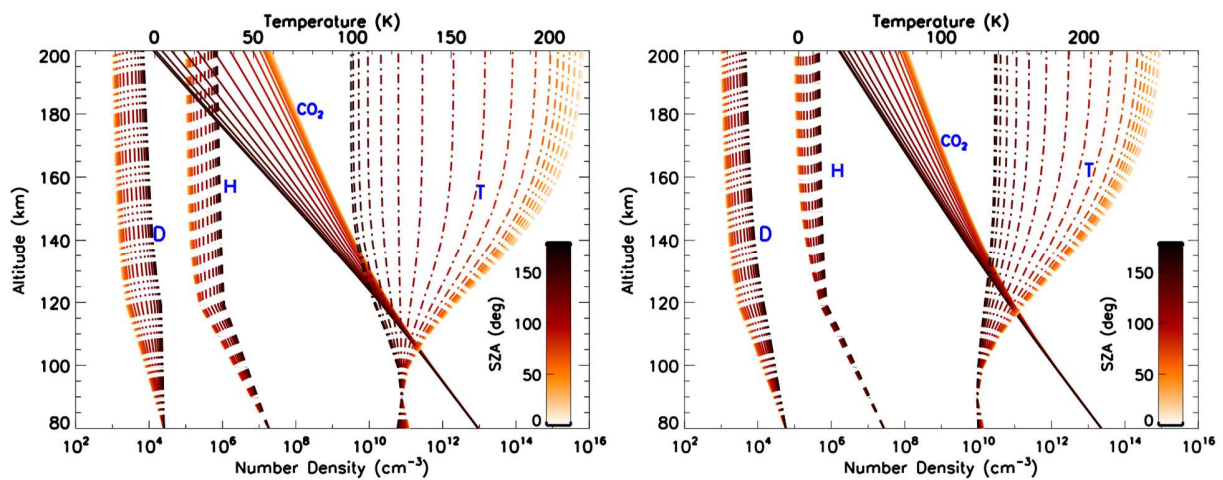
314      2.2.2 *From the homopause to the exobase: 120 – 200 km*

315 The homopause altitude for the martian atmosphere is taken to be at ~120 km in the model  
316 [Krasnopolsky et al., 1998; Nagy et al., 2009; Mahaffy et al., 2015c]. Therefore, the region  
317 between 120 – 200 km has the different species diffusively separated in the atmosphere of Mars.  
318 Since CO<sub>2</sub> is by far the most dominant species at these altitudes, the modeling process considers  
319 only the diffusion of either D or H in CO<sub>2</sub> at these altitudes and utilizes a very simple diffusion  
320 model [Chaufray et al., 2008; Bhattacharyya et al., 2017a] to derive the density of D or H in this  
321 region of the martian atmosphere. However, for the asymmetric, non-isothermal atmosphere the  
322 diffusion equation for deriving deuterium or hydrogen densities is applied at every SZA since the  
323 temperature profile with altitude varies with SZA. The CO<sub>2</sub> profile is derived by applying the  
324 equation of hydrostatic equilibrium at every SZA for a given temperature structure starting from  
325 the lower boundary of the atmosphere (80 km). The CO<sub>2</sub> density at 80 km was determined using a  
326 neutral atmosphere model which utilized a volume mixing ratio at 80 km, consistent with the  
327 relative abundances for CO<sub>2</sub> found in the Mars Climate Database for the temperature profile  
328 derived from NGIMS measurements as described in section 2.1 [Forget et al., 1999; Lewis et al.,  
329 1999]. The model also accounted for molecular and eddy diffusion for interactions of CO<sub>2</sub>  
330 molecules with other neutral species in the martian atmosphere in order to obtain the CO<sub>2</sub> density  
331 at 80 km [Matta et al., 2013; Mayyasi et al., 2019]. This modeling procedure was only applied at  
332 aphelion and perihelion where the exobase temperature and its variation with SZA had been well  
333 established through NGIMS observations. At any other solar longitude, the CO<sub>2</sub> density at 80 km  
334 was determined through sinusoidal interpolation of the CO<sub>2</sub> densities derived at the aphelion ( $L_s =$   
335  $71^\circ$ ) and perihelion ( $L_s = 251^\circ$ ) position of Mars' orbit using eq. (1) where the variables  $y$ ,  $A$  and  
336  $B$  now refer to CO<sub>2</sub> density. The CO<sub>2</sub> density at the lower boundary is kept a constant and is not  
337 varied with SZA in the model as the CO<sub>2</sub> mixing ratios at 80 km used in the model did not show  
338 significant variability with SZA. However, using the mixing ratios in the neutral atmosphere model  
339 did not account for atmospheric variability introduced by pressure differences. Thus, the modeled  
340 CO<sub>2</sub> density profile with altitude obtained from the hydrostatic equilibrium assumption only varies  
341 with SZA due to differences in the temperature profile. The CO<sub>2</sub> density at 80 km was determined  
342 to be  $9.16 \times 10^{12} \text{ cm}^{-3}$  at aphelion and  $2.29 \times 10^{13} \text{ cm}^{-3}$  at perihelion. Appendix B summarizes the  
343 equations applied to this region of the atmosphere in order to derive the density distribution of D  
344 or H.

345       2.2.3 *From the model base to the homopause: 80 – 120 km*

346 At altitudes of 80 – 120 km, the martian atmosphere is well-mixed. In this region, the  
 347 deuterium/hydrogen density distribution was assumed to decrease exponentially with increasing  
 348 altitude constrained by the boundary values at 80 and 120 km. The density at 120 km is estimated  
 349 through the simple diffusion model (Section 2.2.2). For hydrogen, the starting density at 80 km is  
 350 determined by multiplying the H exobase density, which is a free parameter in the model, by a  
 351 ratio (density of hydrogen at 80 km to the exobase density of hydrogen). This ratio is calculated  
 352 from the density profile derived for H at aphelion and perihelion between 80 to 300 km using  
 353 MAVEN-NGIMS derived temperature profile (section 2.1) in conjunction with the same neutral  
 354 atmosphere model which was used to derive the CO<sub>2</sub> density at 80 km. The model accounts for  
 355 hydrogen chemistry in the martian atmosphere and utilized a volume mixing ratio for H at 80 km  
 356 from the Mars Climate Database in order to derive the hydrogen density profile with altitude at  
 357 aphelion and perihelion [Matta et al., 2013]. For all other solar longitudes, the value of this ratio  
 358 is determined by sinusoidally interpolating between the aphelion and the perihelion value using  
 359 eq. (1). This ratio, calculated for hydrogen, is assumed to be the same for deuterium in order to  
 360 satisfy the D/H ratio constraint at Mars. For aphelion, the value of the ratio is determined to be  
 361 ~25 whereas at perihelion the ratio has a value of ~58. Like CO<sub>2</sub>, the densities of H and D at 80  
 362 km are kept constant and do not have any SZA dependence.

363 Figure 2 shows an example of modeled deuterium and hydrogen density profile at  $L_s = 74^\circ$   
 364 and  $L_s = 251.6^\circ$  as well as the corresponding temperature and CO<sub>2</sub> density profile and their  
 365 variation with solar zenith angle. This density profile for D and H was generated for an arbitrary  
 366 exobase density of  $1 \times 10^3 \text{ cm}^{-3}$  for D and  $1 \times 10^5 \text{ cm}^{-3}$  for H at SZA = 0°. This value of exobase  
 367 density for D or H is the only free parameter in the atmosphere model.



368

369 **Figure 2:** Variation of temperature, CO<sub>2</sub> density, hydrogen density and deuterium density with  
 370 altitude and solar zenith angle at a solar longitude  $L_s = 74^\circ$  (left), which is close to aphelion and  
 371  $L_s = 251.6^\circ$  (right), which is close to perihelion, derived using the two-dimensional density model.  
 372 As is evident from the figure, there is significant variation in the different species density and  
 373 temperature between the sub-solar and the anti-solar point in the atmosphere of Mars.

374

### 375 **3. Calculating the line of sight intensity of D and H at Lyman $\alpha$**

376 The solar Lyman  $\alpha$  photons undergo resonant scattering both by the deuterium and the hydrogen  
 377 atoms in the exosphere of Mars. However, the deuterium densities at the martian exobase are  
 378 orders of magnitude lower than hydrogen exobase densities. Therefore, the solar Lyman  $\alpha$  photons  
 379 at 1215.33 Å undergo only single scattering by deuterium atoms at Mars, because of which the  
 380 line of sight Lyman  $\alpha$  intensity recorded at 1215.33 Å is directly proportional to the column  
 381 density of deuterium. This makes it easier to translate the observed intensities into density  
 382 distributions for deuterium in the exosphere of Mars. For hydrogen, the larger densities in  
 383 comparison to deuterium results in multiple scattering of the Lyman  $\alpha$  photons at 1215.67 Å,  
 384 because of which observed line of sight intensities cannot be directly translated into column  
 385 densities. Rigorous radiative transfer modeling is required to interpret the observed intensities in  
 386 order to derive a density distribution for hydrogen. The following sections describe the method by  
 387 which the deuterium and hydrogen Lyman  $\alpha$  intensities were calculated for a given density  
 388 distribution, which can then be used to simulate Mars D and H Lyman  $\alpha$  observations.

#### 389 *3.1 Determining the deuterium Lyman $\alpha$ intensity at 1215.33 Å*

390 For a given deuterium density distribution generated using the two-dimensional atmosphere model  
 391 (Section 2), the intensity along any line of sight passing through the atmosphere was determined  
 392 by calculating the column density along that line of sight and multiplying it by the Lyman  $\alpha$   
 393 excitation frequency at 1215.33 Å (g-value) at Mars. The excitation frequency can be calculated  
 394 using the following relation:

$$395 \quad g = F_0 \times \sigma_0 \times \Delta\lambda_D \times \sqrt{\pi} \quad (6)$$

396 In the above equation  $g$  is the excitation frequency in  $s^{-1}$ ,  $F_0$  the Lyman  $\alpha$  line center flux at Mars  
 397 (photons/cm<sup>2</sup>/s/Å),  $\sigma_0$  the Lyman  $\alpha$  scattering cross section (cm<sup>2</sup>) of deuterium at 1215.33 Å and

398  $\Delta\lambda_D$  the Doppler width of the Mars line ( $\text{\AA}$ ). The value of  $g$  is independent of the gas temperature  
 399 as the temperature dependence of the scattering cross section and the temperature dependence of  
 400 the Doppler width term cancel each other out.

### 401 *3. 2 Determining the hydrogen Lyman $\alpha$ intensity at 1215.67 $\text{\AA}$*

402 The solar Lyman  $\alpha$  photons at 1215.67  $\text{\AA}$  undergo multiple scattering in the hydrogen exosphere  
 403 of Mars. Therefore, a radiative transfer model is required to analyze the optically thick hydrogen  
 404 Lyman  $\alpha$  emissions from the martian exosphere. Earlier modeling efforts were restricted to a  
 405 spherically symmetric and isothermal atmosphere [Anderson and Hord, 1971; Anderson 1974;  
 406 Chaufray et al., 2008; Chaffin et al., 2014; 2015; 2018; Bhattacharyya et al., 2015; 2017a; 2017b].  
 407 From MAVEN and HST observations, it became evident that the hydrogen exosphere is unlikely  
 408 to be spherically symmetric and isothermal [Chaffin et al., 2015; Bhattacharyya et al., 2017a]. The  
 409 MAVEN observations found a  $\sim 100$  K difference in temperature between the sub-solar and anti-  
 410 solar region of the atmosphere [Figure 1; Stone et al., 2018; Mayyasi et al., 2019]. Therefore, a  
 411 two-dimensional radiative transfer model was developed in order to simulate multiple scattering  
 412 in a non-spherically symmetric, and non-isothermal atmosphere, which was then used to analyze  
 413 the MAVEN and HST observations of H Lyman  $\alpha$  emission from Mars. Appendix B describes the  
 414 2-D radiative transfer model in detail. The Lyman  $\alpha$  scattering frequency at 1215.67  $\text{\AA}$  is  
 415 calculated using equation 6. Once the single and multiple scattering source functions have been  
 416 determined from the 2-D radiative transfer model for a given atmosphere, the line of sight H  
 417 Lyman  $\alpha$  intensity can be derived using the following equation:

$$418 \quad I_{\mathcal{H}}(r, \theta, \varphi) = I_{\mathcal{H}}(r_{\infty}, \theta, \varphi)e^{-\tau_{\mathcal{H}}(r, r_{\infty})} + \int_r^{r_{\infty}} S_{\mathcal{H}}(r, \theta, \varphi) e^{-\tau_{\mathcal{H}}(r, r')} ds' \quad (7)$$

419 In the above equation which describes the intensity along a line of sight passing through the  
 420 martian atmosphere,  $r$ ,  $\theta$ , and  $\varphi$  are the three coordinates in the spherical coordinate system,  
 421  $I_{\mathcal{H}}(r_{\infty}, \theta, \varphi)$  is the Lyman  $\alpha$  intensity contribution from external sources like the interplanetary  
 422 hydrogen medium (IPH) or the geocorona,  $e^{-\tau_{\mathcal{H}}(r, r')}$  the total extinction of the Lyman  $\alpha$  photons  
 423 along the line of sight due to absorption by  $\text{CO}_2$  as well as scattering by H atoms present in the  
 424 martian atmosphere and  $S_{\mathcal{H}}(r, \theta, \varphi)$  the total source function or the volume emission rate at a  
 425 particular point in the martian atmosphere due to single and multiple scattering of solar Lyman  $\alpha$   
 426 photons. Lyman  $\alpha$  intensity due to external sources when present is subtracted off from the data



427 either using observations or models for those external sources. For the MAVEN-IUVS limb  
428 observations, the external source was IPH which was estimated using the Pryor model [Pryor et  
429 al., 1992; 2013; Ajello et al., 1987] and subtracted off from the martian hydrogen Lyman  $\alpha$   
430 emission. For the HST observations, a dedicated orbit for every Mars observing visit observed the  
431 blank sky in order to capture the background emission from the IPH and the geocorona. Data from  
432 this orbit was used to remove the background Lyman  $\alpha$  emissions present in the Mars observations.

#### 433 **4. Modeling D and H Lyman $\alpha$ observations with HST and MAVEN**

434 Both the deuterium and the hydrogen Lyman  $\alpha$  emissions at Mars have been extensively observed  
435 with MAVEN and the hydrogen Lyman  $\alpha$  emission with HST and MEX [Clarke et al., 2014; 2017;  
436 Chaffin et al., 2014; 2015; 2018; Bhattacharyya et al., 2015; 2017a; 2017b; Mayyasi et al., 2017b;  
437 2018; 2019; Chaufray et al., 2008]. These observations have been analyzed with the goal of  
438 constraining the present-day H and D escape rates, which are direct tracers of water and bulk  
439 atmospheric escape from Mars throughout its evolution history. While determining the H escape  
440 flux using HST observations, it was noted that several factors increase the uncertainty in the  
441 derived H escape flux values [Bhattacharyya et al., 2017a]. Among them are the absolute  
442 calibration of the instrument and the assumption of a spherically symmetric and isothermal  
443 exosphere in modeling Mars. This section presents an improved absolute calibration for HST and  
444 compares it with MAVEN, as well as presents a comparison of the symmetric vs. asymmetric  
445 model fits to the data.

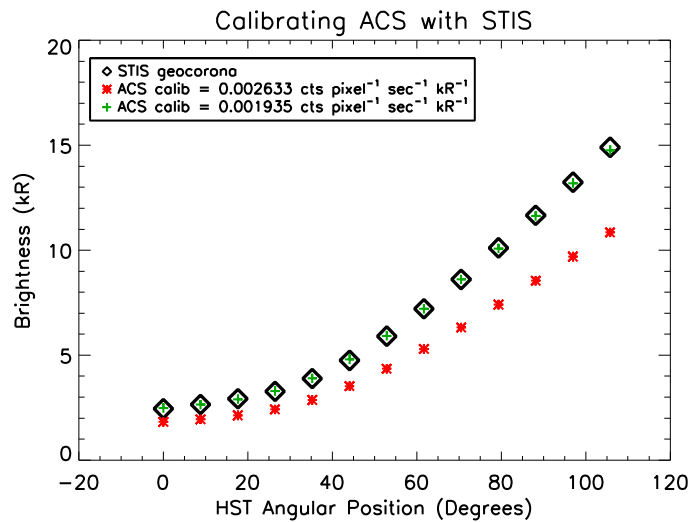
##### 446 *4.1 Absolute Calibration of HST and comparison with MAVEN*

447 The Hubble Space Telescope has been used extensively to study the hydrogen exosphere of Mars  
448 [Clarke et al., 2014; Bhattacharyya et al., 2015; 2017a; 2017b]. Far ultraviolet images of the Lyman  
449  $\alpha$  emission from the martian exosphere have been obtained using the Advanced Camera for  
450 Surveys (ACS) instrument on HST. These images were analyzed to infer the hydrogen escape rates  
451 from the exosphere of Mars. However, the ACS images were obtained by using broadband filters  
452 and therefore the exact sensitivity of the detector at Lyman  $\alpha$  is unknown. This increased the  
453 uncertainty in the derived hydrogen escape flux upon analysis of the data.

454 More recently, an HST observing campaign was conducted with the sole purpose of  
455 calibrating the ACS detector at Lyman  $\alpha$  (1215.67 Å). This calibration campaign utilized the

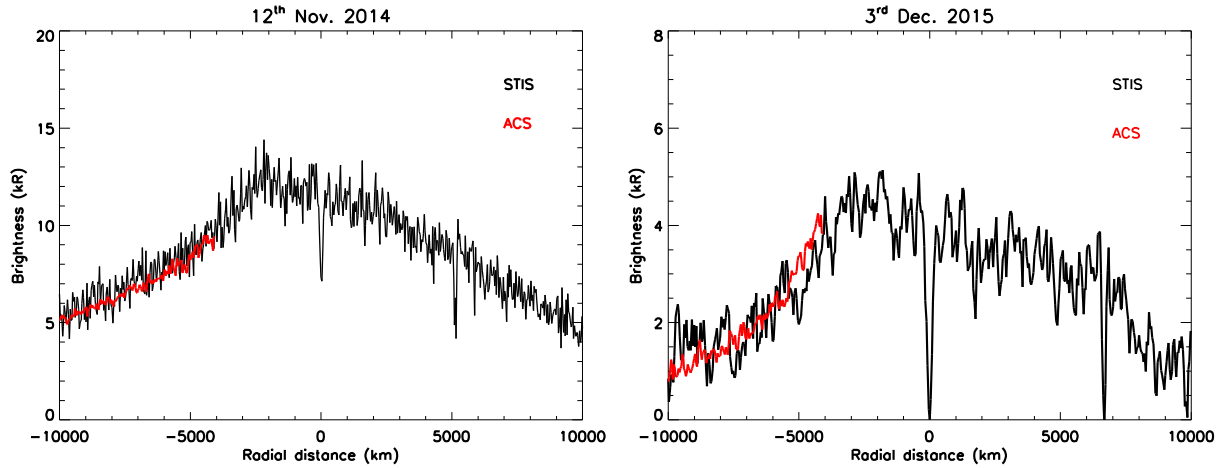
456 Space Telescope Imaging Spectrograph (STIS) instrument whose sensitivity has been well  
 457 calibrated at the Lyman  $\alpha$  wavelength. The STIS instrument was used to observe the geocoronal  
 458 Lyman  $\alpha$  emission for one HST orbit. The same patch of sky was then observed by the ACS  
 459 instrument through the next HST orbit. The geocoronal Lyman  $\alpha$  intensities recorded by the two  
 460 instruments were then compared against each other to derive the absolute calibration of ACS at  
 461 Lyman  $\alpha$ . The new calibration factor for ACS at Lyman  $\alpha$  is  $0.001935 \text{ counts pixel}^{-1} \text{ sec}^{-1} \text{ kR}^{-1}$ .  
 462 This value is 36% smaller than the older theoretically calculated value of  $0.002633 \text{ counts pixel}^{-1} \text{ sec}^{-1} \text{ kR}^{-1}$ .  
 463 Figure 3a shows the comparison between the STIS and the ACS recorded intensities of  
 464 the geocorona using the old calibration factor derived theoretically ( $0.002633 \text{ counts pixel}^{-1} \text{ sec}^{-1} \text{ kR}^{-1}$ ) [Bhattacharyya et al., 2017a] and the new calibration factor of  $0.001935 \text{ counts pixel}^{-1} \text{ sec}^{-1} \text{ kR}^{-1}$   
 465  $\text{kR}^{-1}$  derived through the HST ACS calibration campaign.  
 466

467 The new calibration factor derived for ACS was tested by comparing overlapping  
 468 observations of the martian hydrogen Lyman  $\alpha$  emission obtained using STIS and ACS on 12<sup>th</sup>  
 469 November 2014 and 3<sup>rd</sup> December 2015. Figure 3b shows the comparison between the STIS and  
 470 the ACS intensity of the martian exosphere at  $1215.67 \text{ \AA}$ . The two profiles lie on top of each other  
 471 for both the observing visits thereby validating the new ACS calibration factor.



472  
 473 **Figure 3a:** This figure shows the geocoronal intensities observed by the STIS instrument as well  
 474 as the ACS instrument onboard HST when observing the same patch of the sky with HST's orbital  
 475 position in degrees. The ACS intensities processed using the old calibration factor ( $0.002633$

476 counts  $\text{pixel}^{-1} \text{sec}^{-1} \text{kR}^{-1}$ ) do not match up well with the STIS intensities, whereas, with the new  
477 calibration factor the values recorded by the two instruments overlap completely.



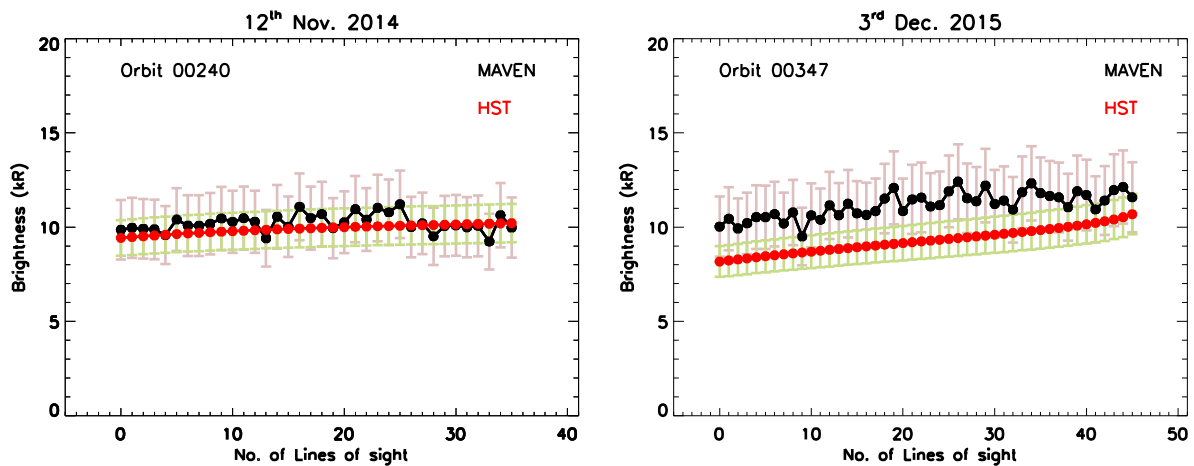
478

479 **Figure 3b:** The above two figures show the brightness of Mars' Lyman  $\alpha$  emission (with the  
480 geocoronal + interplanetary hydrogen background subtracted) as observed by STIS (black) and  
481 ACS (red) on 12<sup>th</sup> November, 2014 and 3<sup>rd</sup> December, 2015. The new calibration factor derived  
482 for ACS was used to determine the brightness of the martian hydrogen exosphere as observed by  
483 ACS for the above two observations. As can be seen in the two figures, the ACS intensities match  
484 those measured by STIS, i.e. the red line (ACS intensity) overlaps with the black line (STIS  
485 intensity) for both observations.

486 Comparison of HST-ACS observed brightness for the martian exosphere with MAVEN is  
487 not a straightforward process. The two instruments have different observing geometry and lines of  
488 sight. The ACS brightness values have to be analyzed and fit to models to obtain the hydrogen  
489 density distribution in the martian exosphere that best matches the data for a particular day of  
490 observation. Using this density distribution, the modeled HST brightness for MAVEN-IUVS  
491 observing geometry can then be derived and compared with the actual brightness recorded by the  
492 MAVEN satellite in orbit around Mars on the same observation date. This comparison study was  
493 conducted for two specific dates, 12<sup>th</sup> November 2014 and 3<sup>rd</sup> December 2015 where there were  
494 corresponding dayside observations available with both HST and MAVEN. For the comparison  
495 study, only disk observations of Mars by the MAVEN-IUVS echelle were used in order to avoid  
496 uncertainties in the modeling process brought on by the presence of interplanetary hydrogen  
497 background in the MAVEN-IUVS signal. Figure 4 shows the comparison between the model

498 derived brightness that would be observed by HST (red points) in MAVEN's observing geometry  
 499 with the actual brightness observed by MAVEN-IUVS echelle (black points). The brightness  
 500 derived from modeling the HST observations and the actual brightness observed by MAVEN are  
 501 within the uncertainty. There is an offset between HST and MAVEN intensities for the 2015  
 502 observations which could be due to an inaccurate derivation of Mars' exospheric characteristics  
 503 from the HST observations because of larger noise in the data (Figure 7) as a result of low count  
 504 rate since Mars was close aphelion during the 2015 observation with the solar activity approaching  
 505 minimum. However, the MAVEN IUVS observational intensities for 3<sup>rd</sup> December 2015 do fall  
 506 within the 10% uncertainty accorded to the model results.

507 A similar comparison study was presented in Mayyasi et al. [2017a] for the 12<sup>th</sup> November  
 508 2014 overlapping observations with MAVEN-IUVS echelle and HST. However, the HST  
 509 observations were reduced using the old calibration factor for ACS and the modeling was done  
 510 using a 1-dimensional radiative transfer model for observed H Lyman  $\alpha$  intensities. The resulting  
 511 comparison with MAVEN was not as accurate as the figure below [figure 4 left].



512  
 513 **Figure 4:** Comparison between the model derived Mars disk brightness that would be observed  
 514 by HST (red points) in MAVEN-IUVS echelle observing geometry with the actual brightness  
 515 observed by MAVEN-IUVS Echelle (black points) on 12<sup>th</sup> November 2014 and 3<sup>rd</sup> December 2015.  
 516 The uncertainty in the brightness observed by MAVEN due to the ~25% uncertainty in absolute  
 517 calibration is represented by the light pink lines whereas the light green lines represent the  
 518 uncertainty in the model derived brightness which is taken to be ~10%.

519 *4.2 Modeling MAVEN and HST observations using an asymmetric atmosphere*

520 MAVEN observations of H and D Lyman  $\alpha$  as well as HST observations of H Lyman  $\alpha$  were  
521 modeled using an asymmetric atmosphere and the 2-D radiative transfer model as described in  
522 sections 2 and 3 respectively. The MAVEN observations with the IUVS-echelle instrument are  
523 restricted to lower tangent altitude ranges between 0 – 300 km, whereas the HST observations  
524 extend from 700 – 30,000 km. The hydrogen exosphere at Mars approaches a more uniform and  
525 spherically symmetric structure above  $\sim 2.5$  martian radii [Holmström, 2006; Bhattacharyya et al.,  
526 2017a]. Therefore, the 2-D model is more important for an accurate analysis and interpretation of  
527 the MAVEN IUVS-echelle observations of the martian H Lyman  $\alpha$  emission.

#### 528 *4.2.1. Modeling MAVEN IUVS-Echelle Observations of Deuterium*

529 MAVEN IUVS-Echelle observations of D Lyman  $\alpha$  between November 2014 – October 2017 have  
530 been analyzed using the 2-D asymmetric model in order to derive best-fit exobase densities for D  
531 (2952 orbits in total), the results of which have been published in Mayyasi et al. [2019]. These  
532 observations have also been previously used to study the seasonal variability of the deuterium  
533 Lyman  $\alpha$  intensity in the martian exosphere [Clarke et al., 2017; Mayyasi et al., 2017]. In this  
534 paper, a detailed description of the modeling process supporting the data analysis is presented.

535 For modeling the MAVEN IUVS-Echelle observations of D, first the exobase temperatures are  
536 pre-determined by interpolating NGIMS observations at aphelion and perihelion for all the  
537 MAVEN-IUVS echelle orbits (section 2.1). Then the 2-D atmosphere model was used to produce  
538 density distributions for a total of 7 different exobase densities, 100, 500, 1000, 3000, 5000, and  
539  $7000 \text{ cm}^{-3}$  at SZA of  $0^\circ$  for every MAVEN IUVS echelle orbit ( $2952 \times 7 = 20664$  atmospheres  
540 simulated). For each model atmosphere corresponding to a particular MAVEN IUVS echelle orbit,  
541 the line of sight deuterium Lyman  $\alpha$  intensity was calculated by deriving the column density along  
542 that line of sight and multiplying it by the excitation frequency of Lyman  $\alpha$  at  $1215.33 \text{ \AA}$  (eq.6).

543 The line integrated solar Lyman  $\alpha$  at  $1215.67 \text{ \AA}$  flux is measured by the Extreme Ultraviolet  
544 Monitor (EUVM) instrument onboard the MAVEN orbiter at Mars [Eparvier et al., 2015]. It has a  
545 full width half max (FWHM) of  $1 \text{ \AA}$  and therefore encompasses the solar Lyman  $\alpha$  flux at  $1215.33$   
546  $\text{ \AA}$ . From the EUVM measurements of the line integrated flux, the Lyman  $\alpha$  flux at line center  
547 ( $1215.67 \text{ \AA}$ ) was calculated by using the widely-used Emerich relationship [Emerich et al., 2005].  
548 Based on the shape of the Lyman  $\alpha$  profile, the solar Lyman  $\alpha$  flux at  $1215.33 \text{ \AA}$  is derived, which

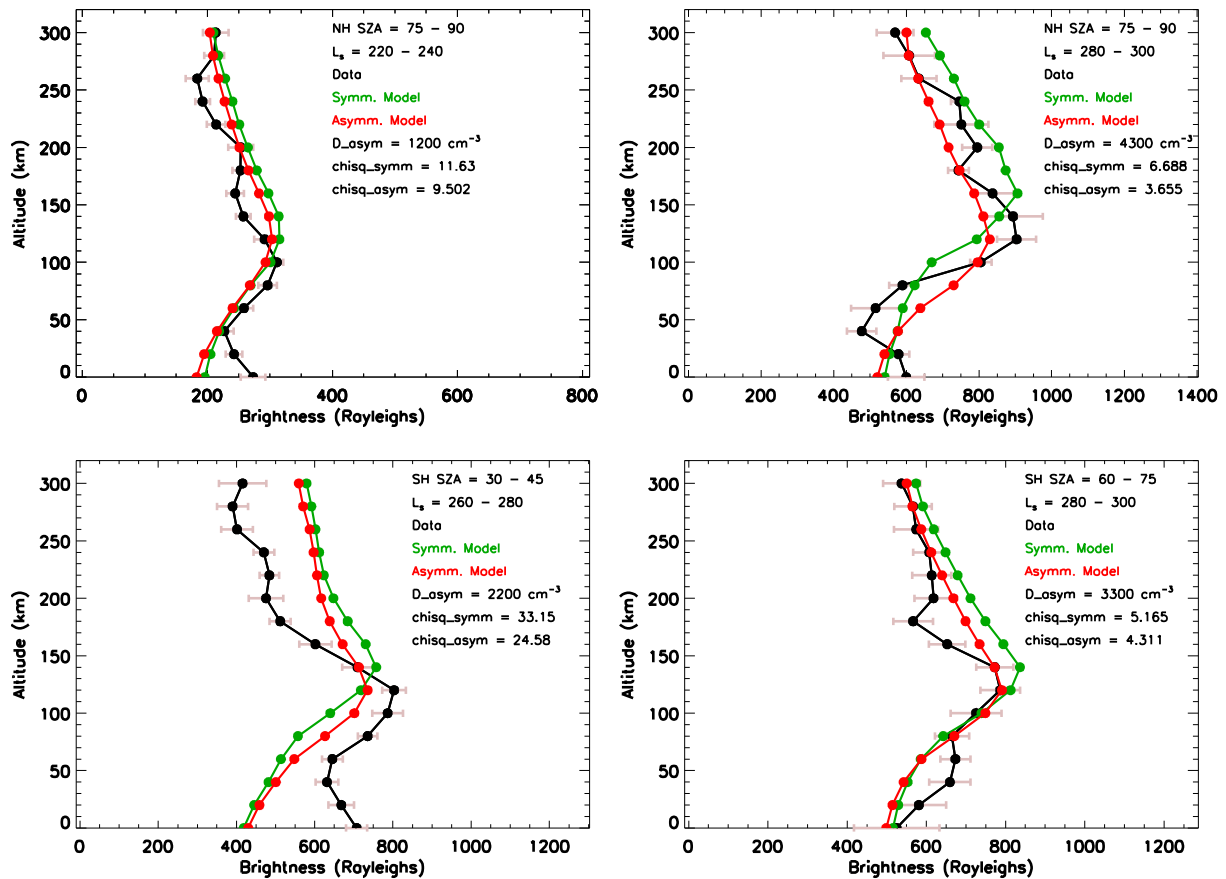
549 is almost the same as the flux at line center (greater by  $\sim 1.6\%$ ), and this value is used in determining  
550 the excitation frequency of Lyman  $\alpha$  at  $1215.33 \text{ \AA}$  for all the MAVEN-IUVS echelle orbits.

551 Since the deuterium signal is faint at Mars, the data was binned into  $L_s$ , SZA and altitude bins  
552 to obtain intensity profiles with altitude for deuterium. Six  $L_s$  bins were created with  $20^\circ$  spacing  
553 within solar longitudes  $220^\circ - 340^\circ$ , four SZA bins were created between  $30^\circ - 90^\circ$  with  $15^\circ$  spacing  
554 and twenty one altitude bins were created between  $0 - 400 \text{ km}$  with  $20 \text{ km}$  spacing as elaborated  
555 in Mayyasi et al., [2019]. The model followed the same binning scheme as the data using the 2952  
556 orbits to produce simulated intensity profiles with altitude which can then be compared to the data.  
557 These modeled intensity profiles derived for the seven different exobase densities were then  
558 linearly interpolated on a more refined exospheric density grid to obtain the best fit exospheric  
559 density of deuterium that matched the data through the process of  $\chi^2$  minimization.

560 Figure 5 shows the comparison between the best fit modeled density to the data for deuterium  
561 as measured by IUVS echelle using the spherically symmetric model, which assumes an isothermal  
562 symmetric atmosphere [Bhattacharyya et al., 2017a], and the spherically asymmetric model  
563 described here. The figure shows four cases for available dayside solar zenith angles for the  
564 northern hemisphere (top two plots) and the southern hemisphere (bottom two plots) as observed  
565 by the IUVS echelle instrument onboard MAVEN [Mayyasi et al., 2019]. In all cases the  
566 asymmetric model fits the data better than the symmetric model for the exobase density displayed  
567 in the respective figures. However, even the asymmetric model fails to provide perfect fits to the  
568 data, especially at lower altitudes. This is because the D signal is above the detection threshold of  
569 the MAVEN-IUVS detector only between  $L_s = 220^\circ - 340^\circ$  and the dataset presented in figure 5,  
570 which was analyzed and reported in Mayyasi et al. [2019], has dayside coverage of that solar  
571 longitude range only during late 2014 – early 2015. During this time MAVEN had just started its  
572 science phase and the optimal conditions like detector gain, binning scheme, observing geometry,  
573 etc. for recording the D emission from the martian exosphere had not yet been established, thereby  
574 degrading the quality of the data collected. It is expected that more IUVS observations of the D  
575 emissions through multiple perihelion passages of Mars in the future would provide better model  
576 fits to the data.

577 An advantage of the asymmetric model is that it allows analysis and comparison of IUVS  
578 observations at different solar zenith angles under the same solar longitude and solar activity  
579 conditions using a single model run in order to better constrain the asymmetric nature of Mars'

580 exosphere. Presently, this has not been possible for D due to the lack of observations [Mayyasi et  
 581 al., 2019]. But with IUVS's continued observations of the D Lyman  $\alpha$  emission with every  
 582 perihelion passage of Mars, this would soon be possible.



583  
 584 **Figure 5:** This figure displays the symmetric and asymmetric model fits to the IUVS-Echelle  
 585 deuterium observation for a predetermined exobase temperature from MAVEN-NGIMS  
 586 observations and an exobase density at SZA =  $0^\circ$  as displayed in the figures. The exobase density  
 587 varied with SZA following the Hodges and Johnson [1968] formulation for the asymmetric model,  
 588 but remained constant for the symmetric model. The top two plots are for the northern hemisphere  
 589 and the bottom two plots are for the southern hemisphere. These simulations are for an MAVEN-  
 590 NGIMS measured aphelion temperature of 216 K and a perihelion temperature of 255 K [Mayyasi  
 591 et al., 2019].

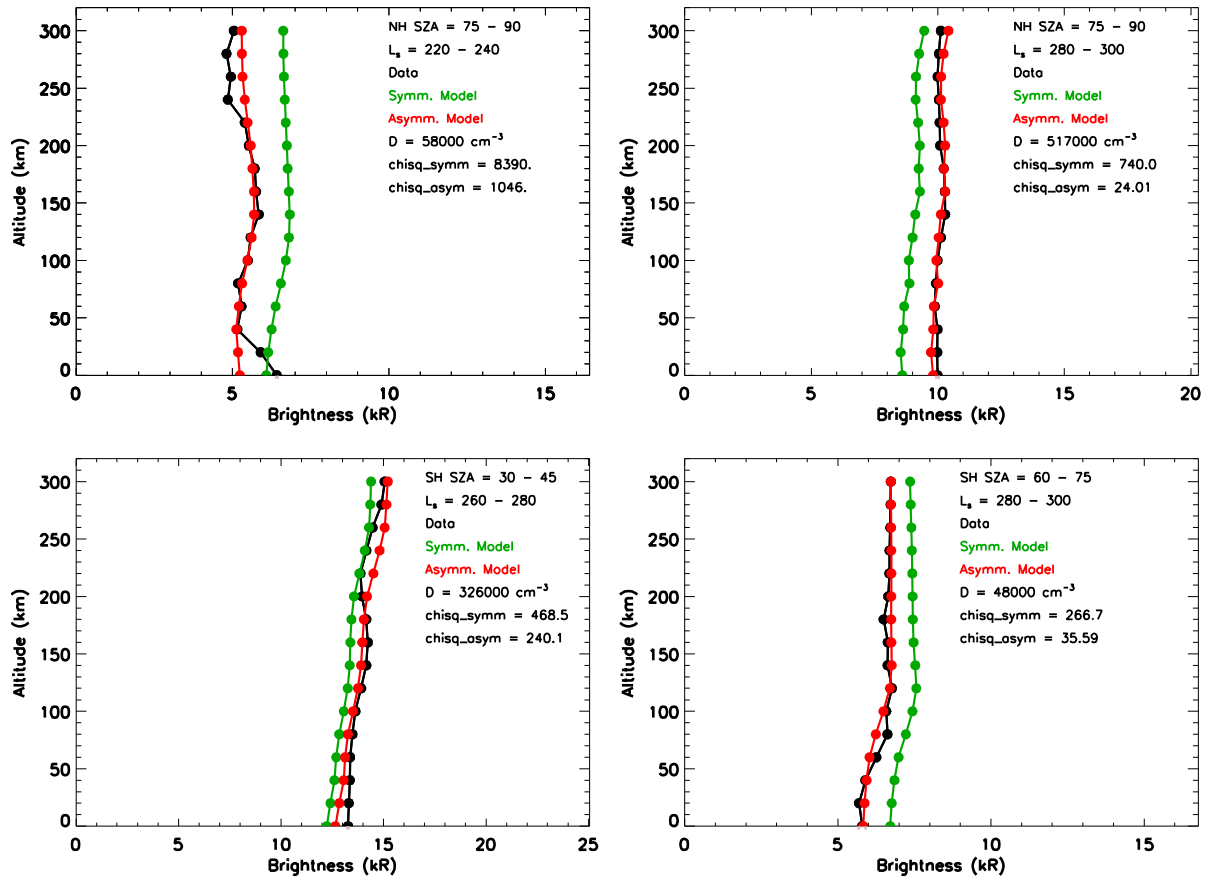
592 4.2.2. Modeling MAVEN IUVS-Echelle Observations of Hydrogen

593 MAVEN observations of H Lyman  $\alpha$  between November 2014 – October 2017, simultaneously  
594 observed with the D Lyman  $\alpha$  emission by the IUVS echelle instrument, have been utilized in this  
595 study (2952 orbits in total). Some of the observations have been previously used to study the  
596 seasonal variability of hydrogen in the martian exosphere as well as the response of the H escape  
597 rate to solar flare events [Clarke et al., 2017; Mayyasi et al., 2018]. For modeling the MAVEN  
598 observations of hydrogen, the 2-D radiative transfer model (Appendix B) in conjunction with the  
599 2-D atmosphere model (section 2; Appendix A) was used to determine the emissivity for a range  
600 of exobase densities for thermal hydrogen ( $10^4 - 7 \times 10^5 \text{ cm}^{-3}$ ; 13 different exobase density values)  
601 at Mars' aphelion and perihelion positions (26 simulations with the 2-D atmosphere + RT model).  
602 The exobase temperatures at perihelion and aphelion positions were pre-determined by averaging  
603 NGIMS observations of the lower thermosphere conducted over a period of  $\sim 1.5$  Mars years  
604 (section 2). The emissivity of Mars' atmosphere for all the MAVEN-IUVS echelle orbits (2952  
605 orbits in total) for each exobase was calculated by sinusoidally interpolating the emissivity  
606 determined at aphelion and perihelion using the 2-D RT model using eq. 1. The Lyman  $\alpha$  line  
607 center flux at  $1215.67 \text{ \AA}$  in the model was determined from EUVM measurements of the line  
608 integrated flux which were then converted to line center flux using Emerich's analytical formula  
609 [Emerich et al., 2005]. Next, the line of sight hydrogen Lyman  $\alpha$  intensity for each MAVEN-IUVS  
610 echelle orbit was calculated using equation 7. The model results were then binned into solar  
611 longitudes, SZA and altitude bins, same as the deuterium observations to facilitate D/H  
612 calculations which will be published in a future study. This modeled and observed intensity  
613 profiles were compared and the density that best matched the data was determined through the  
614 process of  $\chi^2$  minimization. Non-thermal hydrogen was not considered in the modeling process  
615 because the altitude profiles are restricted to line of sight altitudes below  $\sim 3000$  km, where the  
616 thermal component is dominant.

617 Figure 6 shows the comparison between MAVEN IUVS echelle measurements of H Lyman  $\alpha$   
618 emission and the best modeled fit to the data using the asymmetric model and the symmetric  
619 model. This figure displays the corresponding H Lyman  $\alpha$  emission to the D Lyman  $\alpha$  emission  
620 measured by the IUVS echelle instrument displayed in figure 5. The error bars are larger for the  
621 fainter D Lyman  $\alpha$  emission than for the much brighter and easily detectable H Lyman  $\alpha$  emission.  
622 Unlike the D observations, the H Lyman  $\alpha$  observations above the limb include a contribution from  
623 the interplanetary hydrogen (IPH). The IPH intensity was estimated using the widely used Pryor



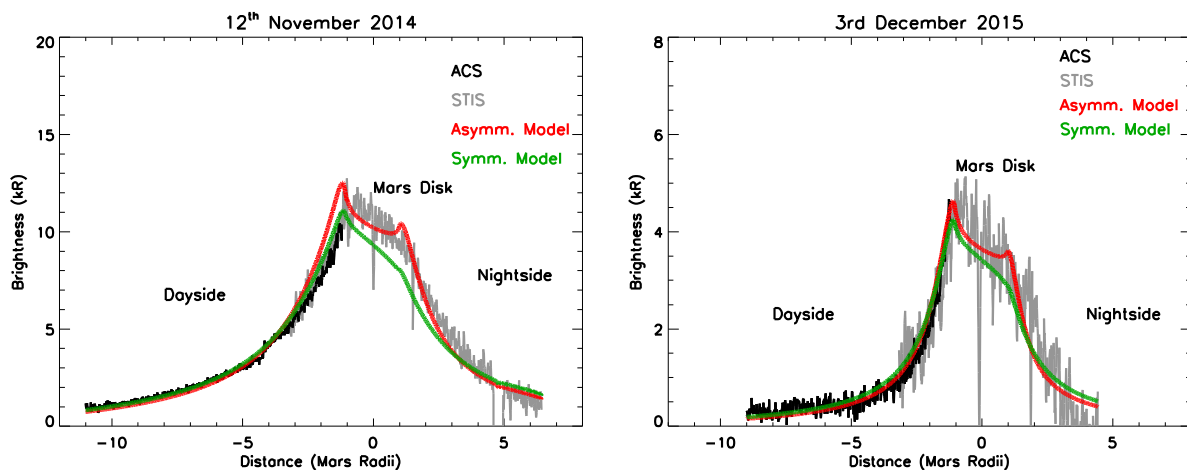
624 model [Pryor et al., 1992; 2013; Ajello et al., 1987]. As is evident from the figure, the asymmetric  
 625 model provides a better fit to the data than the symmetric model for the exobase density displayed  
 626 in the respective figures.



627  
 628 **Figure 6:** This figure displays the symmetric and asymmetric model fits to the IUVS-Echelle  
 629 hydrogen observations for a predetermined exobase temperature from MAVEN-NGIMS  
 630 observations and an exobase density at  $SZA = 0^\circ$  as displayed in the figures. The exobase density  
 631 varied with SZA following the Hodges and Johnson [1968] formulation for the asymmetric model,  
 632 but remained constant for the symmetric model. The top two plots are for the northern hemisphere  
 633 and the bottom two plots are for the southern hemisphere. These simulations are for an MAVEN-  
 634 NGIMS measured aphelion temperature of 216 K and a perihelion temperature of 255 K [Mayyasi  
 635 et al., 2019].

636 4.2.3. Modeling HST Observations of Hydrogen

637 Two sets of HST observations obtained on 12<sup>th</sup> November 2014 and 3<sup>rd</sup> December 2015 were  
638 modeled using the 2-D atmosphere + radiative transfer model as well as the 1-D atmosphere +  
639 radiative transfer model and the comparison between the two model results were studied. On the  
640 above-mentioned observation dates, Mars was imaged using two different instruments on the HST,  
641 i.e., ACS and STIS. The ACS instrument was used to image the highly extended dayside hydrogen  
642 exosphere of Mars. The ACS images for the martian Lyman  $\alpha$  emission are a difference between  
643 two images obtained with the F115LP filter, which transmits Lyman  $\alpha$ , and the F140LP filter,  
644 which blocks Lyman  $\alpha$  but allows emissions up to 140 nm wavelengths. Therefore, the disk of  
645 Mars in the final differenced image is noisy on account of other emissions like oxygen 130.4 nm  
646 and the 135.6 nm emissions and solar continuum. However, above  $\sim 700$  km the hydrogen Lyman  
647  $\alpha$  emission becomes dominant. Therefore, the ACS observations capture the Mars H Lyman  $\alpha$   
648 profile accurately above  $\sim 700$  km. The STIS observations, on the other hand, can spectrally isolate  
649 the Lyman  $\alpha$  emission from the Mars disk. Thus, both ACS and STIS observations of Mars were  
650 combined together to obtain the martian H Lyman  $\alpha$  intensity profile from the dayside to the night  
651 side including the disk. Background emissions from the interplanetary hydrogen (IPH) and the  
652 geocorona in the Mars observations were estimated using a dedicated HST orbit as a part of each  
653 visit which observed the background blank sky 5 arcminutes away from Mars for the same portion  
654 of HST's orbit as the Mars observations with STIS and ACS. The estimated background intensity  
655 was then subtracted off from the Mars H Lyman  $\alpha$  data. Figure 7 shows the final Mars H Lyman  
656  $\alpha$  profile obtained for the two observation days.



657

658 **Figure 7:** *Asymmetric and symmetric model fits to HST observations of the martian exospheric*  
659 *hydrogen Lyman  $\alpha$  emission observed on 12<sup>th</sup> November 2014 and 3<sup>rd</sup> December 2015. The data*  
660 *consists of dayside exospheric observations with the ACS instrument along with the martian disk*  
661 *and night side observations with the STIS instrument onboard HST. The asymmetric model fits the*  
662 *disk and the night side intensities better than the symmetric model. The differences between the*  
663 *asymmetric and the symmetric model intensities become small above  $\sim 2.5$  martian radii suggesting*  
664 *that the martian hydrogen exosphere approaches symmetry at higher altitudes.*

665 For modeling the HST observations using the 2-D RT model, first the 2-D density model  
666 was used to generate density profiles with thermal hydrogen exobase densities at SZA =  $0^\circ$  ranging  
667 from  $1 \times 10^4 \text{ cm}^{-3}$  –  $5 \times 10^5 \text{ cm}^{-3}$  (11 different density values). The exobase temperature at SZA =  
668  $0^\circ$  for the two observation days were taken from the Mars Global Circulation Model (MGCM)  
669 [Chaufray et al., 2015; 2018]. MAVEN-NGIMS observations were not used here because  
670 MAVEN's orbit on these days did not sample close to the sub-solar point. The 2-D RT model was  
671 then used to simulate the emissivity of the atmosphere for each exobase density. The thermal H  
672 density that best matches the STIS observation up to  $\sim 2000$  km through least-squares minimization  
673 was used to determine the thermal H population for that particular HST observation. The  
674 superthermal population of H atoms was determined through the same method as used in previous  
675 HST observation analysis [Bhattacharyya et al. 2015; 2017a; 2017b]. The temperature of the H  
676 superthermal population was taken to be 800 K. Different exobase densities for superthermal H  
677 ranging from  $1 \times 10^3 \text{ cm}^{-3}$  –  $4 \times 10^4 \text{ cm}^{-3}$  were added to the best-fit thermal density profile and the  
678 emissivity of the atmosphere was then determined using the 2-D RT model. The density of the  
679 superthermal population of H was not varied with SZA. The best-fit non-thermal density was then  
680 determined through chi-square minimization of the model fits to the ACS intensity profile, which  
681 extends from  $\sim 700$  km to  $\sim 30,000$  km and contains emissions from superthermal H atoms which  
682 become significant at higher altitudes (above  $\sim 20,000$  km). Table 1 lists the best-fit thermal and  
683 superthermal H densities and temperatures for the two HST observation days. These values were  
684 then used in a symmetric 1-D model where the temperature and density varied only radially and  
685 not with SZA to simulate the intensity from a spherically symmetric and isothermal atmosphere.  
686 Figure 7 shows the comparison between the output from the symmetric and the asymmetric model  
687 for both the 12<sup>th</sup> November 2014 observation as well as the 3<sup>rd</sup> December 2015 observation of the  
688 martian hydrogen Lyman  $\alpha$  emission HST. As is evident from the figure, the asymmetric model

689 fits the data better than the symmetric model, especially the disk brightness and the night side  
690 brightness for the martian H corona. However, differences between the symmetric and the  
691 asymmetric model intensities decrease above an altitude of  $\sim 2.5$  martian radii as the martian  
692 hydrogen exosphere approaches symmetry in conjunction with previous studies [Holmström,  
693 2006; Bhattacharyya et al., 2017a; Chaufray et al., 2015]. The Jeans escape flux derived from the  
694 symmetric model fits are greater than the asymmetric model fits to the data by a factor of 1.5 and  
695 1.87 for the two HST observations.

696 **Table 1:** *Modeled characteristics of the hydrogen exosphere for the HST observations*

| Date of Observation<br>(day of year) | Exobase temperature of thermal H at SZA = $0^\circ$<br>$T_{\text{cold}}$ (K) | Exobase density of thermal H at SZA = $0^\circ$<br>$N_{\text{cold}}$ ( $\text{cm}^{-3}$ ) | Exobase temperature of energetic H<br>$T_{\text{hot}}$ (K) | Exobase density of energetic H<br>$N_{\text{hot}}$ ( $\text{cm}^{-3}$ ) | Thermal H escape (atoms/sec)   |                                |
|--------------------------------------|--|---|--|---|--------------------------------|--------------------------------|
|                                      |  |   |  |   | Asymmetric model               | Symmetric model                |
| 12 <sup>th</sup> November 2014 (316) | 300  | $189000 \pm 4000$   | 800  | $10000 \pm 2000$  | $6.23 \pm 0.14 \times 10^{26}$ | $9.32 \pm 0.2 \times 10^{26}$  |
| 3 <sup>rd</sup> December 2015 (337)  | 250  | $79000 \pm 4000$  | 800  | $5000 \pm 4000$   | $8.54 \pm 0.44 \times 10^{25}$ | $1.59 \pm 0.08 \times 10^{26}$ |

697

## 698 5. Summary and Discussion

699 Observations and analysis of the martian exospheric Lyman  $\alpha$  emission in the past decade have  
700 slowly revealed the complicated nature of this tenuous upper atmospheric layer. The presence of  
701 a superthermal H component have been inferred from the analysis of Mars Express (MEX), HST  
702 and MAVEN observations [Chaufray et al., 2008; Chaffin et al., 2014; 2015; Clarke et al., 2014;  
703 Bhattacharyya et al., 2015]. These observations also revealed that the exosphere is not spherically  
704 symmetric and isothermal [Holmström, 2006; Chaffin et al., 2015; Bhattacharyya et al., 2017a].

705 MAVEN-NGIMS observations of the lower thermosphere reported temperature differences of >  
706 100 K between the day and the night side indicating a non-isothermal exosphere [Stone et al.,  
707 2018] and models imply a large difference in H density between subsolar and anti-solar point  
708 [Chaufray et al., 2018]. Therefore, in this study a more physically accurate 2-dimensional model  
709 of the martian exosphere based on MAVEN findings was constructed which would provide better  
710 constraints on the present-day escape rates of deuterium and hydrogen atoms from the exosphere  
711 of Mars. It is imperative to obtain an accurate value for the escape rate of H as it is tied to the  
712 escape of water from Mars, whereas an accurate estimate of the D/H ratio will help establish the  
713 timeline for the escape of the martian atmosphere throughout its history of evolution.

714           Uncertainties in estimating the D and H escape rate arise from both uncertainties in the  
715 data as well as the modeling process as was concluded from the Bhattacharyya et al. [2017] study.  
716 The data uncertainties are mostly dominated by the uncertainty in the instrumental absolute  
717 calibration [Bhattacharyya et al., 2017a]. A recent HST observation campaign utilized the STIS  
718 instrument onboard HST, whose absolute calibration is well-documented (within 5%) through  
719 observations of standard UV stellar sources, to determine the sensitivity of the ACS instrument at  
720 Lyman  $\alpha$ . The ACS instrument, which is a broadband filter, has been used to image the H Lyman  
721  $\alpha$  emission from many different planetary hydrogen coronae, including Mars. Therefore,  
722 calibrating the ACS detector at Lyman  $\alpha$  will help reduce the uncertainties associated with  
723 determining the H escape rate from Mars through analysis of HST ACS observations. The  
724 MAVEN-IUVS echelle Lyman  $\alpha$  calibration factor was cross-checked with overlapping HST  
725 observations. However, the observed martian H Lyman  $\alpha$  intensity by the MAVEN-IUVS echelle  
726 cannot be directly compared to the intensities recorded by HST due to the differences in their  
727 observing geometry. A 2-D radiative transfer model was utilized to obtain the characteristics of  
728 the martian hydrogen exosphere (hydrogen exobase density and temperature) for a particular day  
729 of observation (12<sup>th</sup> November 2014 and 3<sup>rd</sup> December 2015). This “best-fit” atmosphere for that  
730 particular day of observation was then used to simulate the H Lyman  $\alpha$  intensities that would be  
731 observed by HST from the MAVEN-IUVS echelle observing geometry on that day. Assuming a  
732 10% uncertainty in the modeling process, the MAVEN observed intensity, with its present  
733 calibration factor (including a 25% uncertainty), lies within the HST simulated intensity limits.

734           Model uncertainties are a result of the various assumptions made in the simulation process  
735 about the characteristics of the martian exosphere. Earlier models assumed a spherically symmetric

736 and isothermal exosphere. However, observations in the past decade have indicated an asymmetric  
737 non-isothermal exosphere below ~5000 km (~1.5 martian radii from the surface). Most of the  
738 spacecraft observations (MEX, and MAVEN) of the martian H and D Lyman  $\alpha$  emissions are  
739 conducted at those altitudes. Therefore, in order to model the spacecraft observations a two-  
740 dimensional density model and a two-dimensional radiative transfer model was developed through  
741 this study. The density and temperature of the exospheric species were varied with altitude and  
742 solar zenith angle. This asymmetric model was then tested against results from the symmetric  
743 model by simulating MAVEN-IUVS Echelle observations of D and H Lyman  $\alpha$  and HST  
744 observations of H Lyman  $\alpha$  at Mars. In all cases the asymmetric model fit the data as well or better.  
745 The asymmetric model is particularly important for the comparison of observations at very  
746 different solar zenith angles, as is the case for the MAVEN mission.

747 For the HST observations, the asymmetric model better simulated the disk and the night  
748 side intensities than the symmetric model. The models converged above ~2.5 martian radii.  
749 Disparities between the 2-D model and the data below 2.5 martian radii could be due to local  
750 asymmetries in atmospheric characteristics that are not captured in the modeling process. Elevated  
751 densities for helium (by a factor of about 10 – 20) have been detected by MAVEN on the night  
752 side compared to the dayside [Elrod et al., 2017]. A larger concentration of helium was also  
753 detected in the polar regions compared to the equatorial regions. Similar asymmetries in H  
754 densities have been difficult to detect due to the optically thick nature of the Lyman  $\alpha$  emission as  
755 well as the large expanse of the hydrogen exosphere. For D, the density is not large enough in the  
756 exosphere during most of the martian year ( $L_s = 330^\circ$ -  $220^\circ$  through aphelion at  $L_s = 71^\circ$ ) to  
757 generate a Lyman  $\alpha$  intensity which is detectable above the MAVEN-IUVS echelle detection  
758 threshold of ~100 Rayleighs. Therefore, MAVEN observations collected over the past 1.5 Mars  
759 years cannot detect large anomalies in densities. MAVEN orbit also precesses slowly around Mars  
760 in latitude and local solar time due to which only one perihelion ( $L_s = 251^\circ$ ) and southern summer  
761 solstice ( $L_s = 270^\circ$ ) coverage of the dayside deuterium emission was available in the dataset  
762 utilized in this study. This data is from late 2014 to early 2015 when MAVEN had just undergone  
763 its orbit insertion around Mars. The MAVEN-IUVS echelle observing geometries, integration  
764 times and detector binning schemes ideal for observing D and H Lyman  $\alpha$  had not yet been  
765 established thereby resulting in degradation of the D Lyman  $\alpha$  data. All these factors together could  
766 contribute towards the mismatch between the data and the 2-D model presented in this paper.

767 Jeans escape flux estimates for H from the HST simulations as listed in table 1 indicate that  
768 a spherically symmetric model could overestimate the escape fluxes by more than a factor of 1.5.  
769 Similar estimates have not been provided for D and H from the IUVS observations as the data is  
770 heavily binned and contains a mixture of observations spanning from November 2014 – October  
771 2017. In conclusion, the results of this study do establish that an asymmetric model is required to  
772 simulate the D and H Lyman  $\alpha$  emissions from the exosphere of Mars in order to better constrain  
773 the total amount of water/atmospheric that has escaped Mars in its ~4.5 billion years of existence,  
774 an important research goal currently being pursued by the Mars science community.

775

## 776 **Acknowledgements**

777 The first author thanks Jordan Montgomery and Sabyasachi Chatterjee for helpful discussions  
778 about the mathematical derivations presented in the Vidal-Madjar and Bertaux [1972] paper. This  
779 work was supported by NASA contract no. 1000320450 from the University of Colorado to Boston  
780 University as well as Space Telescope Science Institute (STScI) grant GO-15098 to Boston  
781 University. All HST data used in this study can be downloaded from the Space Telescope Science  
782 Institute server at <http://archive.stsci.edu/hst/search.php> and all MAVEN data used in this study  
783 are available on the NASA Planetary Data System at [https://pds.nasa.gov/datasearch/subscription-](https://pds.nasa.gov/datasearch/subscription-service/SS-20180215.shtml)  
784 [service/SS-20180215.shtml](https://pds.nasa.gov/datasearch/subscription-service/SS-20180215.shtml) for release 12 of the IUVS level1a and level1c echelle dataset.

785

## 786 **Appendix A**

### 787 *A.1. Density distribution in a non-uniform and non-isothermal exosphere (above 200 km)*

788 The Chamberlain [1963] approach for deriving exospheric density distributions is a 1-dimensional  
789 (1D) approach which assumes spherical symmetry. This approach was extended to 2-D/3-D by  
790 Vidal-Madjar and Bertaux [1972] which is applicable to a non-spherically symmetric density  
791 distribution in a planetary exosphere. Since collisions are negligible in the exosphere, the particles  
792 still obey Liouville's theorem and follow the Maxwell-Boltzmann velocity distribution. For such  
793 an asymmetric atmosphere, the distribution function at the critical altitude or the exobase is given  
794 by:

795 
$$f_c(\alpha_c, \delta_c, V_c) = N_c(\alpha_c, \delta_c) \left[ \frac{1}{2\pi m k_b T_c(\alpha_c, \delta_c)} \right]^{3/2} \exp \left[ \frac{-mMGV_c^2}{r_c k_b T_c(\alpha_c, \delta_c)} \right] \quad (\text{A1.1})$$

796 Here  $N_c(\alpha_c, \delta_c)$  is the number density at the exobase as a function of the longitude,  $\alpha_c$  and latitude,  
 797  $\delta_c$ ,  $m$  the mass of the species,  $k_b$  the Boltzmann's constant,  $T_c(\alpha_c, \delta_c)$  the exobase temperature  
 798 which is also a function of longitude and the latitude,  $r_c$  the exobase altitude (200 km for Mars),  
 799  $V_c$  the velocity at the exobase normalized to the escape velocity,  $M$  the mass of the planet and  $G$   
 800 the universal gravitational constant. Defining the following variables:

801 
$$y = \frac{r_c}{r} \qquad V = \frac{v}{v_{esc}}$$

802 In the above expressions,  $r$  is an arbitrary radial distance from planet center and  $v_{esc} = \sqrt{\frac{2GM}{r_c}}$ .

803 The equations of motion of the particles in the collisionless exospheric regime which obey the law  
 804 of conservation of energy and angular momentum can be written as:

805 
$$V_c^2 - 1 = V^2 - y \quad (\text{A1.2})$$

806 
$$\frac{v \sin \theta}{y} = V_c \sin \theta_c \quad (\text{A1.3})$$

807 The number density at any point in space can now be written as,

808 
$$N(y, \alpha, \delta) = v_{esc}^3 \int N_c(\alpha_c, \delta_c) \left[ \frac{m}{2\pi k_b T_c(\alpha_c, \delta_c)} \right]^{3/2} \exp \left[ \frac{-mMG(V^2+1-y)}{r_c k_b T_c(\alpha_c, \delta_c)} \right] V^2 \sin \theta dV d\theta d\varphi \quad (\text{A1.4})$$

809 The above equation comes from Liouville's theorem which states that the density in phase space  
 810 is conserved along dynamical trajectories. The integration is in momentum space over  $V$ ,  $\theta$ , and  $\varphi$   
 811 which are restricted to the existing trajectories that the particles might follow in the exosphere.

812 There are three different types of trajectories that the particles can take which are,

- 813
  - Ballistic trajectories where  $V_c < 1$  or  $V < \sqrt{y}$  with all the trajectories intersecting the
- 814 exobase
- 815
  - Escaping trajectories where  $V_c > 1$  and  $V > \sqrt{y}$
- 816
  - Satellite trajectories which are created by small number of collisions which may take place
- 817 between particles in the exosphere. The particles which follow the satellite trajectories are
- 818 still bound by the planet's gravity and their trajectories do not cross the exobase level.

819 Since the number of collisions taking place in the exosphere is negligible, the total number of  
 820 satellite particles present in the exosphere are considered to be negligible and has been ignored  
 821 while modeling the martian exosphere.



822 *A.1.1 Ballistic Particles*

823 There is a velocity  $V_b$  at every radial distance  $r$  such that if  $V < V_b$ , the corresponding trajectory  
 824 of the particle will intersect the exobase for any direction of the velocity vector. This velocity  $V_b$   
 825 corresponds to a trajectory whose apogee is  $r$  and perigee is  $r_c$  with  $\sin \theta = \sin \theta_c = 1$ . Applying  
 826 this to equations (A1.2) and (A1.3) we have:

827 
$$V_b = \frac{y}{\sqrt{1+y}} \quad (\text{A1.5})$$

828 If  $V > V_b$ , then all trajectories do not reach the exobase. Only those trajectories which lie within  
 829 a cone of half-angle  $\theta_m$  whose axis is the local vertical, will have their perigees intersecting the  
 830 exobase. With  $\theta = \theta_m$  and  $\sin \theta_c = 1$  in equations (A1.2) and (A1.3) we have:

831 
$$\sin \theta_m = \frac{y}{V} \sqrt{V^2 + 1 - y} \quad (\text{A1.6})$$

832 The ascending particles populate the region  $0 < \theta < \theta_m$ , whereas the descending particles  
 833 populate the region  $\pi - \theta_m < \theta < \pi$ . The number density of ballistic particles at any radial  
 834 distance will have the expression,

835 
$$N_b(y, \alpha, \delta) = v_{esc}^3 \int_0^{V_b} \int_0^\pi \int_0^{2\pi} f_c V^2 \sin \theta dV d\theta d\varphi +$$
  
 836 
$$v_{esc}^3 \int_{V_b}^{\sqrt{y}} \int_0^{\theta_m} \int_0^{2\pi} f_c V^2 \sin \theta dV d\theta d\varphi + v_{esc}^3 \int_{V_b}^{\sqrt{y}} \int_{\pi-\theta_m}^\pi \int_0^{2\pi} f_c V^2 \sin \theta dV d\theta d\varphi \quad (\text{A1.7})$$

837 The distribution function  $f_c$  has no  $\theta$  or  $\varphi$  dependence and is only a function of the variables  
 838  $V_c$ , and  $\alpha_c, \delta_c$  through  $N_c(\alpha_c, \delta_c)$  and  $T_c(\alpha_c, \delta_c)$  dependence. Thus, in order to solve the above  
 839 integral, first  $\alpha_c$  and  $\delta_c$  needs to be calculated and then the terms  $N_c(\alpha_c, \delta_c)$  and  $T_c(\alpha_c, \delta_c)$  need  
 840 to be evaluated using the known functional dependence of the exobase density and temperature on  
 841 the solar zenith angle. The density model presented here is only in 2-D. Therefore, in the modeling  
 842 process the latitude  $\delta = 0^\circ$  which now renders the longitude angle  $\alpha$  as the solar zenith angle. The  
 843 variables  $\alpha_c$  and  $\delta_c$  is calculated using the following equations:

844 
$$\delta_c(\alpha, \delta, \varphi, \psi) = \sin^{-1}(\cos \delta \sin \psi \cos \varphi + \sin \delta \cos \psi) \quad (\text{A1.8})$$

845 
$$\psi = \beta - \beta_c \quad \beta = \cos^{-1} \left( \frac{y\omega(y,V,\theta) - r_c}{e(y,V,\theta)} \right) \quad \beta_c = \cos^{-1} \left( \frac{\omega(y,V,\theta) - r_c}{e(y,V,\theta)} \right)$$

846 
$$\omega = 2r_c \frac{V^2 \sin^2 \theta}{y^2} \quad e = \sqrt{1 - \frac{4V^2 \sin^2 \theta (y - V^2)}{y^2}}$$

847 
$$\alpha_c(\alpha, \delta, \varphi, \psi) = \cos^{-1} \left( \frac{-\sin \delta \cos \alpha \sin \psi \cos \varphi + \sin \alpha \sin \psi \sin \varphi + \cos \delta \cos \alpha \cos \psi}{\cos \delta_c(\alpha, \delta, \varphi, \psi)} \right) \quad (\text{A1.9})$$

848 The solar zenith angle can be written as  $\gamma = \cos^{-1}(\cos \alpha_c \cos \delta_c)$  and because of the symmetry  
 849 in the 3<sup>rd</sup> dimension,  $N_c(\alpha_c, \delta_c) = N_c(\gamma)$  and  $T_c(\alpha_c, \delta_c) = T_c(\gamma)$ .

### 850 *A.1.2 Escaping Particles*

851 Under this condition, all trajectories which result in escape from the parent body's gravitational  
 852 potential are considered. These trajectories also lie within a cone of half-angle  $\theta_m$  ( $0 < \theta < \theta_m$ ),  
 853 the expression for which is given by the relation depicted in equation (A1.6). The number density  
 854 of escaping particles at any radial distance from the planet's center is given by the expression:

$$855 \quad N_e(y, \alpha, \delta) = v_{esc}^3 \int_{\sqrt{y}}^{\infty} \int_0^{\theta_m} \int_0^{2\pi} f_c V^2 \sin \theta dV d\theta d\varphi \quad (\text{A2.0})$$

856 The distribution function  $f_c$  has no  $\theta$  or  $\varphi$  dependence and is only a function of the variable  
 857  $V_c$ , and  $\alpha_c, \delta_c$  through  $N_c(\alpha_c, \delta_c)$  and  $T_c(\alpha_c, \delta_c)$  dependence, same as the ballistic particle case.

858

### 859 *A.2. Density distribution below 200 km*

860 The density distribution below the exobase is estimated using a simple diffusion model in which  
 861 only the diffusion of H or D in CO<sub>2</sub> is considered [Bhattacharyya et al., 2017a]. The diffusion  
 862 equation from Hunten [1973] is of the form:

$$863 \quad \Phi_H(r) = -(D_H + K) \frac{dn_H}{dr} - \left[ D_H \left( \frac{GMm_H}{kT(r)r^2} + \frac{1+\alpha_T}{T} \frac{dT}{dr} \right) + K \left( \frac{GM\mu}{kT(r)r^2} + \frac{1}{T} \frac{dT}{dr} \right) \right] n_H \quad (\text{A2.1})$$

864 In the above equation,  $D_H$  is the diffusion coefficient of H or D in CO<sub>2</sub> given by  $D_H(r) = \frac{AT(r)^s}{n_{CO_2}(r)}$ ,

865  $A = 8.4 \times 10^{17} \text{ cm}^2 \text{ s}^{-1}$  for H and  $A = 1.0 \times 10^{17} \text{ cm}^2 \text{ s}^{-1}$  for D;  $s = 0.6$  for H and  $s = 0.75$  for D  
 866 [Hunten, 1973].  $K$  is the eddy diffusion co-efficient and has the expression  $K(h) =$

867  $1.2 \times 10^{12} \sqrt{\frac{T_\infty}{n(h)}} \text{ cm}^2 \text{ s}^{-1}$  [Krasnopolsky, 2002]. The thermal coefficient factor  $\alpha_T$  equals -0.25

868 for both H and D (Krasnopolsky, 2002). Upon solving the diffusion equation for each SZA, the  
 869 number density with altitude and SZA can be derived for either D or H at Mars [Chaufray et al.,  
 870 2008; Bhattacharyya et al., 2017a].

## 871 **Appendix B**

### 872 *B.1. Radiative transfer model for a non-symmetric, non-isothermal atmosphere*

873 A photon when it passes through a medium, its characteristics such as wavelength, frequency and  
874 direction of propagation, may be altered because of interaction with the medium. The process of  
875 radiative transfer and the relevant equations describe the physical process governing the interaction  
876 of the photon with the surrounding medium. The solution of these equations applied to a specific  
877 problem provides the means of accurately simulating the radiation field in various environments.  
878 In this section, the radiative transfer process in a non-spherically symmetric and non-isothermal  
879 environment is explored and the relevant equations that describe this process are derived.

880 The general equation of radiative transfer in a medium is given by the relation:

$$881 \quad \frac{dI_\nu(\mathbf{r}, \theta, \varphi)}{ds} = -\kappa_\nu^{ext}(\mathbf{r}) I_\nu(\mathbf{r}, \theta, \varphi) + S_\nu(\mathbf{r}, \theta, \varphi) \quad (\text{B1.1})$$

882 In the above equation,  $I_\nu(\mathbf{r}, \theta, \varphi)$  is the intensity (photons  $\text{cm}^{-2} \text{s}^{-1} \text{Hz}^{-1} \text{sr}^{-1}$ ),  $S_\nu(\mathbf{r}, \theta, \varphi)$  the volume  
883 emission rate or source function (photons  $\text{cm}^{-3} \text{s}^{-1} \text{sr}^{-1} \text{Hz}^{-1}$ ) and  $\kappa_\nu^{ext}(\mathbf{r})$  the extinction coefficient  
884 ( $\text{cm}^{-1}$ ) which is a sum of the scattering and absorption coefficients. The formal solution to equation  
885 (B1.1) as presented by Chandrasekhar [1960] can be written as:

$$886 \quad I_\nu(\mathbf{r}, \theta, \varphi) = I_\nu(\mathbf{r}_\infty, \theta, \varphi) e^{-\tau_\nu(\mathbf{r}, \mathbf{r}_\infty)} + \int_{\mathbf{r}}^{\mathbf{r}_\infty} S_\nu(\mathbf{r}', \theta, \varphi) e^{-\tau_\nu(\mathbf{r}, \mathbf{r}')} ds' \quad (\text{B1.2})$$

887 In the above equation which describes the intensity along a line of sight through a medium, the  
888 term  $I_\nu(\mathbf{r}_\infty, \theta, \varphi)$  describes the contribution to the line of sight intensity from sources external to  
889 the medium, the term  $e^{-\tau_\nu(\mathbf{r}, \mathbf{r}_\infty)}$  describes the attenuation of the line of sight intensity (scattering  
890 and absorption within the medium as well as external to the medium), the term  $S_\nu(\mathbf{r}', \theta, \varphi)$  is the  
891 source function due to scattering of photons within the medium and  $e^{-\tau_\nu(\mathbf{r}, \mathbf{r}')}$  the attenuation  
892 (scattering and absorption) within the medium. In the absence of external sources, the above  
893 equation reduces to:

$$894 \quad I_\nu(\mathbf{r}, \theta, \varphi) = \int_{\mathbf{r}}^{\mathbf{r}_\infty} S_\nu(\mathbf{r}', \theta, \varphi) e^{-\tau_\nu(\mathbf{r}, \mathbf{r}')} ds' \quad (\text{B1.3})$$

895 The source function term is a combination of scattering from internal and external sources.

$$896 \quad S_\nu(\mathbf{r}, \theta, \varphi) = S_\nu^{ext}(\mathbf{r}, \theta, \varphi) + S_\nu^{int}(\mathbf{r}, \theta, \varphi)$$

897 Internal sources of radiation like photoelectron impact excitation, etc. are ignored in the modeling  
898 process presented in this paper. The external source function has the form:

$$899 \quad S_\nu^{ext}(\mathbf{r}, \theta, \varphi) = \frac{b}{4\pi} \int_0^\infty dv' \kappa_{\nu'}^{sca}(\mathbf{r}) \int d\Omega' R(\mathbf{r}; \nu, \nu', \Omega, \Omega') I_\nu(\mathbf{r}_\infty, \theta', \varphi') e^{-\tau_{\nu'}(\mathbf{r}, \mathbf{r}_\infty)} \quad (\text{B1.4})$$

900 In the above equation,  $b$  is the branching ratio for the transitions from the excited upper state to  
901 the ground state,  $\kappa_{\nu'}^{sca}(\mathbf{r})$  the scattering coefficient,  $d\Omega'$  the angular element in which the resonant  
902 scattering occurs,  $R(\mathbf{r}; \nu, \nu', \Omega, \Omega')$  the scattering redistribution function,  $I_\nu(\mathbf{r}_\infty, \theta', \varphi')$  the

903 intensity of the incident radiation at the top of the atmosphere, and  $e^{-\tau_{v'}(\mathbf{r}, \mathbf{r}_\infty)}$  the attenuation due  
 904 to absorption and scattering of the incident radiation along a line of sight.

905 If the medium is optically thick, then the external source term is a combination of the single  
 906 and multiple scattering source function. In the case of Mars, the hydrogen exosphere resonantly  
 907 scatters solar Lyman  $\alpha$  photons. Therefore, the single scattering term will merely describe the  
 908 scattering of the solar Lyman  $\alpha$  photons by the martian hydrogen exosphere. The single scattering  
 909 source function for the process of resonant scattering of solar photons by martian H atoms can be  
 910 written as:

$$911 \quad S_v^{Sun}(\mathbf{r}, \theta, \varphi) = b \int_0^\infty dv' \kappa_{v'}^{sca}(\mathbf{r}) \int d\Omega' R(\mathbf{r}; v, v', \Omega, \Omega_{Sun}) \pi F_{Sun}(v') e^{-\tau_{v'}(\mathbf{r}, \mathbf{r}_{Sun})} \quad (B1.5)$$

912 Isotropic scattering of the solar photons is considered which reduces  $\int d\Omega' =$   
 913  $\int_0^\pi \sin \theta' d\theta' \int_0^{2\pi} d\varphi' = 4\pi$  and removes the  $\Omega$  dependency from the redistribution function.  
 914 Therefore,  $R(\mathbf{r}; v, v', \Omega, \Omega_{Sun}) = R(\mathbf{r}; v, v')$ .

915 The atmosphere considered in the model is symmetric in the  $\varphi$  direction in the spherical  
 916 polar coordinate system, but is variable in the  $\mathbf{r}$  and  $\theta$  direction. Here forth, the variable  $\mathbf{r}$  in the  
 917 equations will represent dependency in both the  $r$  (radial) and  $\theta$  (SZA) direction. The sun is taken  
 918 to be along the  $z$  axis in the model. Therefore,  $\theta$  represents the solar zenith angle in the model.

919 For solving equation (B1.5) for a non-symmetrical, non-isothermal atmosphere, we define  
 920 the following variables:

$$921 \quad x(\mathbf{r}) = \frac{v-v_0}{\Delta v_D(\mathbf{r})} \quad (B1.6a); \quad dv = dx \Delta v_D(\mathbf{r}) \quad (B1.6b); \quad \Delta v_D(\mathbf{r}) = \frac{v_0}{c} \sqrt{\frac{2k_b T(\mathbf{r})}{m}} \quad (B1.6c)$$

922 Define a constant reference temperature  $T_{ref}$ , which corresponds to the highest temperature  
 923 value for the entire atmosphere for a particular day. Therefore, the terms in equations (B1.6a),  
 924 (B1.6b) and (B1.6c) will have their reference counterparts, which has no dependence on  $r$ , since  
 925  $T_{ref}$  is a constant. Now, writing the variables  $x(\mathbf{r})$ , and  $\Delta v_D(\mathbf{r})$  in terms of the reference  
 926 temperature, we have:

$$927 \quad x(\mathbf{r}) = x_{ref} \sqrt{\frac{T_{ref}}{T(\mathbf{r})}} \quad (B1.7a); \quad \Delta v_D(\mathbf{r}) = \Delta v_{D,ref} \sqrt{\frac{T(\mathbf{r})}{T_{ref}}} \quad (B1.7b)$$

928 Also, the scattering cross section can now be written as:

$$929 \quad \sigma_0(\mathbf{r}) = \sigma_{ref} \sqrt{\frac{T_{ref}}{T(\mathbf{r})}} \quad (B1.8) \quad \text{where, } \sigma_{ref} = \frac{5.96 \times 10^{-12}}{\sqrt{T_{ref}}}$$

930 Now, expanding upon each of the terms in equation (B1.5):

931  $b = 1$  for resonant scattering of Lyman  $\alpha$  photons by H atoms.

932  $dv' = dx' \Delta v_D(\mathbf{r})$  which is derived from equation (B1.6b).

933  $\kappa_{\nu'}^{SCA}(\mathbf{r}) = n(\mathbf{r}) \sigma_0(\mathbf{r}) e^{-x'^2(\mathbf{r})}$ , where  $\kappa_{\nu'}^{SCA}(\mathbf{r})$  represents the resonant scattering cross section  
 934 and  $n(\mathbf{r})$  the number density at any point  $\mathbf{r}$  in the atmosphere.

935  $R(\mathbf{r}; \nu, \nu') = R(x, x') = \frac{1}{\pi} e^{-x'^2} e^{-x^2}$ ; This function is related to Hummer's [Hummer, 1962] by

936 
$$R(x, x') = \frac{\frac{1}{\pi} e^{-x'^2} e^{-x^2}}{\frac{1}{\pi \Delta v_D(\mathbf{r})} \int_{-\infty}^{\infty} dx e^{-x'^2} e^{-x^2}} \text{ and } \int_{-\infty}^{\infty} e^{-x^2} = \sqrt{\pi}.$$

937  $R(x, x') = \frac{e^{-x^2(\mathbf{r})}}{\sqrt{\pi} \Delta v_D(\mathbf{r})}$ , is the final form of the redistribution function. This form of the function  
 938 considers the process of complete frequency redistribution which is true for moderately thick  
 939 resonance lines and is applicable to the martian Lyman  $\alpha$  emission.

940  $\pi F_{Sun}(\nu') = F_0 = \text{constant}$ , represents the solar Lyman  $\alpha$  flux at line center for a particular day.

941 In general, this flux should vary with frequency, but for Mars the Lyman  $\alpha$  emission line is  
 942 extremely narrow due to the cold atmospheric temperatures and the majority of the H atoms only  
 943 scatter near the line center where the variation of flux with frequency is negligible.

944  $e^{-\tau_{\nu'}(\mathbf{r}, r_{Sun})}$  represents the sum of scattering by H atoms as well as the absorption by CO<sub>2</sub> of the  
 945 Lyman  $\alpha$  photons in the martian atmosphere along any line of sight. The absorption and the  
 946 scattering terms can be written as:

947 absorption by CO<sub>2</sub>:  $e^{-\tau_{CO_2}(\mathbf{r}, r_{Sun})} = \exp\{-\int_r^{r_{Sun}} n_{CO_2}(\mathbf{r}') \sigma_{CO_2}(\mathbf{r}') ds'\}$ . The cross section of  
 948 absorption of Lyman  $\alpha$  photons by CO<sub>2</sub> is dependent upon temperature and does not have any  
 949 analytical formula. However, laboratory measurements exist for the same [Venot et al., 2018].

950 Scattering by H:  $\exp\{-\int_r^{r_{Sun}} n(\mathbf{r}') \sigma_0(\mathbf{r}') e^{-x'^2(\mathbf{r}')} ds'\}$

951 Substituting these expressions in equation (B1.5) we have:

952 
$$\frac{S_x^{Sun}(\mathbf{r})}{\Delta v_D(\mathbf{r})} = \frac{F_0 \Delta v_D(\mathbf{r}) n(\mathbf{r}) \sigma_0(\mathbf{r})}{\sqrt{\pi} \Delta v_D(\mathbf{r})} e^{-\tau_{CO_2}(\mathbf{r}, r_{Sun})} e^{-x^2(\mathbf{r})}$$

953 
$$\times \int_{-\infty}^{\infty} dx' e^{-x'^2(\mathbf{r})} \exp\{-\int_r^{r_{Sun}} n(\mathbf{r}') \sigma_0(\mathbf{r}') e^{-x'^2(\mathbf{r}')} ds'\} \quad (\text{B1.8})$$

954 Upon integrating over  $x$  on both sides,

955 
$$\int_{-\infty}^{\infty} S_x^{Sun}(\mathbf{r}) = S_0^{Sun}(\mathbf{r}); \quad \text{and} \quad \int_{-\infty}^{\infty} dx e^{-x^2(\mathbf{r})} = \sqrt{\pi}$$

956 Therefore, equation (B1.8) reduces to

957  $S_0^{Sun}(\mathbf{r}) =$

958  $g n(\mathbf{r}) e^{-\tau_{CO_2}(\mathbf{r}, r_{Sun})} \frac{1}{\sqrt{\pi}} \int_{-\infty}^{\infty} dx' e^{-x'^2(\mathbf{r})} \exp \left\{ - \int_r^{r_{Sun}} n(\mathbf{r}') \sigma_0(\mathbf{r}') e^{-x'^2(\mathbf{r}')} ds' \right\}$  (B1.9)

959 In the above equation  $g$  is the excitation frequency given by equation  $g = \sqrt{\pi} \Delta v_{D_{ref}} \sigma_{ref} F_0$ .

960 Every  $x$  term and  $\sigma$  term in equation (B1.9) can be written in terms of their reference temperature

961 counterpart using equations (B1.7a, B1.7b and B1.8) which leaves the source function to be

962 dependent on temperature and density, both of which vary with  $r$  and  $\theta$ .

963 For the multiple scattering source function, which is derived from equation (B1.4) has the

964 form:

965  $S_v^{mult}(\mathbf{r}) = \frac{b}{4\pi} \int_0^\infty dv' \kappa_{v'}^{SCA}(\mathbf{r}) \left\{ \int d\Omega' R(\mathbf{r}; v, v') \int_r^{r_\infty} S_{v'}(\mathbf{r}') e^{-\tau_{v'}(\mathbf{r}, \mathbf{r}')} ds' \right\}$  (B2.0)

966 In the above equation the term  $S_{v'}(\mathbf{r}')$ , which has a dependence on frequency  $v$ , can be written as:

967  $S_{v'}(\mathbf{r}') = S(\mathbf{r}') \frac{e^{-x'^2(\mathbf{r})}}{\sqrt{\pi} \Delta v_D(\mathbf{r})}$

968 The forms of the various terms are already known from calculating the single scattering source

969 function. However, unlike for the single scattering source function, the  $\int d\Omega'$  term does not reduce

970 to  $4\pi$ . Substituting the various terms in equation (B2.0) we have:

971  $\frac{S_x^{Mult}(\mathbf{r})}{\Delta v_D(\mathbf{r})} = n(\mathbf{r}) \sigma_0(\mathbf{r}) \left( \int \frac{d\Omega'}{4\pi} \frac{e^{-x^2(\mathbf{r})}}{\sqrt{\pi}} \int_{-\infty}^{\infty} dx' e^{-x'^2(\mathbf{r})} \right.$

972  $\times \left. \left( \int_r^{r_\infty} ds' S(\mathbf{r}') \frac{e^{-x'^2(\mathbf{r}')}}{\sqrt{\pi} \Delta v_D(\mathbf{r}')} e^{-\tau_{CO_2}(\mathbf{r}, \mathbf{r}')} \exp \left\{ - \int_{r_i}^{r_j} n(\mathbf{r}'') \sigma_0(\mathbf{r}'') e^{-x''^2} ds \right\} \right) \right)$  (B2.1)

973 Taking the integral of  $x$  on both sides, the above equation reduces to the following:

974  $S_0^{mult}(\mathbf{r}) = n(\mathbf{r}) \sigma_{ref} \left( \int \frac{d\Omega'}{4\pi} \int_r^{r_\infty} ds' S(\mathbf{r}') e^{-\tau_{CO_2}(\mathbf{r}, \mathbf{r}')} \sqrt{\frac{T_{ref}}{T(\mathbf{r}')}} \right.$

975  $\times \left. \frac{1}{\sqrt{\pi}} \int_{-\infty}^{\infty} dx' e^{-x'^2(\mathbf{r})} e^{-x'^2(\mathbf{r}')} \exp \left\{ - \int_{r_i}^{r_j} n(\mathbf{r}'') \sigma_0(\mathbf{r}'') e^{-x''^2} ds \right\} \right)$  (B2.2)

976 With the expressions for the single and multiple scattering source functions, the total source

977 function at any point  $\mathbf{r}$  in the atmosphere can be written as:

978  $S_{tot}(\mathbf{r}) = S_0^{Sun}(\mathbf{r}) + S_0^{mult}(\mathbf{r})$  (B2.3)

979 The multiple scattering source function has the term  $S(\mathbf{r}')$  in it which prevents the derivation of

980 an analytical expression for the total source function. In order to solve the above equation, an

981 iterative approach is undertaken, where the first term is taken to be the zero-order solution  
 982 [Bertaux, 1974; Quémerais and Bertaux, 1993]. Under this approach, equation (B2.3) is discretized  
 983 and represented by the vectorial relation:

$$984 \quad \vec{S}_{n+1} = \vec{S}_0 + [A] \cdot \vec{S}_n \quad (B2.4)$$

985 In the above equation  $\vec{S}_{n+1}$  is the vector containing the source function values at all the grid points  
 986 in the atmosphere after  $n + 1$  iterations,  $\vec{S}_0$  is the vector containing the single scattering source  
 987 function at all the grid points,  $[A]$  is the matrix of influence which contains information on the  
 988 influence of all the grid points on every grid point due to the process of multiple scattering and  $\vec{S}_n$   
 989 represents the total scattering source function (single and multiple) at all the grid points after the  
 990  $n^{\text{th}}$  iteration. The matrix of influence is given by the expression:

$$991 \quad a_{ij} \\
 992 \quad = \sum_{\Omega_{ij}} \sigma_{ref} n_i \frac{d\Omega_{ij}}{4\pi} e^{-\tau_{CO_2ij}} \sqrt{\frac{T_{ref}}{T(\mathbf{r}_{ij})}} \frac{1}{\sqrt{\pi}} \int_{-\infty}^{\infty} dx_i e^{-x_i^2} e^{-x_j^2} \exp \left\{ - \int_{r_i}^{r_k} n_{ik} \sigma_{0ik} e^{-x_{ik}^2} ds_k \right\} ds_j \\
 993 \quad (B2.5)$$

994 The dimensionless coefficient  $a_{ij}$  represents the contribution to the source function at grid point  $j$   
 995 due to multiple scattering at grid point  $i$ .  $d\Omega_{ij}$  is the solid angle within which point  $i$  sees point  $j$ .  
 996 The iteration represented in equation (B2.4) is conducted until convergence is achieved which is  
 997 determined by the condition:

$$998 \quad \frac{\|\vec{S}_{n+1} - \vec{S}_n\|}{\|\vec{S}_{n+1}\|} \leq \delta = 1 \times 10^{-5} \quad (B2.6)$$

999 The norm of the vector indicates the maximum value for the vector.

1000

## 1001 **References**

- 1002 Ajello, J., A. I. Stewart, G. Thomas, A. Graps (1987), Solar cycle study of interplanetary Lyman-  
 1003 alpha variations – Pioneer Venus orbiter sky background results, *J. Astrophys.*, 317, p. 964 – 986.
- 1004 Anderson, D. E., and C.W. Hord (1971), Mariner 6 and 7 Ultraviolet Spectrometer Experiment:  
 1005 Analysis of Hydrogen Lyman-Alpha Data, *J. Geophys. Res.*, 76, 6666-6673
- 1006 Anderson, D. E., Hord C. W. (1972), Correction. *J. Geophys. Res.*, 77,5638

1007 Anderson, D. E. (1974), Mariner 6, 7 and 9 Ultraviolet Spectrometer Experiment: Analysis of  
1008 Hydrogen Lyman Alpha Data, *J. Geophys. Res.*, *79*, 1513-1518

1009 Babichenko, S.I., Deregusov, E. V., Kurt, V. G., Romanova, N. N., Skljankin, V. A., Smirnov, A.  
1010 S., J.- L. Bertaux, J. Blamont (1977), Measurements in Interplanetary Space and in the martian  
1011 Upper Atmosphere with a Hydrogen Absorption-cell Spectrophotometer for L-alpha Radiation  
1012 On-board Mars 4-7 Space probes, *Space Science Instrumentation*, vol. 3, p. 271-286

1013 Barth, C., W. Fastie, C. Hord, J. Pearce, K. Kelly, A. Stewart, G. Thomas, G. Anderson, O. Raper  
1014 (1969), Mariner 6 Ultraviolet Spectrum of Mars Upper Atmosphere. *Science* *165*, 1004-1005

1015 Bertaux, J. L. (1974), L'hydrogène atomique dans l'exosphère terrestre : mesures d'intensité et  
1016 de largeur de raie de l'émission Lyman-alpha à bord du satellite OGO-5 et interprétation, Ph.D.  
1017 Thesis, University of Paris 6 Pierre et Marie Curie.

1018 Bertaux, J. L., Clarke, J. T., Mumma, M. J., Owen, T., Quemerais, E. (1993), A Search for the  
1019 Deuterium Lyman-alpha Emission from the Atmosphere of Mars, in “*Science with the Hubble*  
1020 *Space Telescope*”, ESO Proc. No. 44, 459-462

1021 Bhattacharyya, D., J. T. Clarke, J. L. Bertaux, J. Y. Chaufray, M. Mayyasi (2015), A Strong  
1022 Seasonal Dependence in the Martian Hydrogen Exosphere, *Geophys. Res. Lett.*, *42*, p. 8678-8685.

1023 Bhattacharyya, D., J. T. Clarke, J. L. Bertaux, J. Y. Chaufray, M. Mayyasi (2017a), Analysis and  
1024 Modeling of Remote Observations of the Martian Hydrogen Exosphere, *Icarus*, *281*, p. 264-280.

1025 Bhattacharyya, D., J. T. Clarke, J. Y. Chaufray, M. Mayyasi, J. L. Bertaux, M. S. Chaffin, N. M.  
1026 Schneider, G. L. Villanueva (2017b), Seasonal Changes in Hydrogen Escape from Mars Through  
1027 Analysis of HST Observations of the Martian Exosphere Near Perihelion, *J. Geophys. Res.*, *122*,  
1028 p. 11756-11764.

1029 Bougher, S., D. Pawlowski, J. Bell, S. Nelli, T. McDunn, J. Murphy, M. Chizek, and A. Ridley (  
1030 2015), Mars Global Ionosphere-Thermosphere Model: Solar cycle, seasonal, and diurnal  
1031 variations of the Mars upper atmosphere, *J. Geophys. Res.: Planets*, *120*, p. 311-342.

1032 Chaffin, M. S., Chaufray, J. Y., Stewart, I., Montmessin, F., Schneider, N. M., Bertaux, J. L.  
1033 (2014), Unexpected Variability of Martian Hydrogen Escape, *Geophys. Res. Lett.*, *41*, 314-320.



1034 Chaffin, M. S., et al. (2015), Three-dimensional structure in the Mars H corona revealed by IUVS  
1035 on MAVEN, *Geophys. Res. Lett.*, *42*, p. 9001-9008.

1036 Chaffin, M. S., J. Deighan, N. Schneider, A. I. F. Stewart (2017), Elevated atmospheric escape of  
1037 atomic hydrogen from Mars induced by high-altitude water, *Nature Geoscience*, *10*, p. 174-178.

1038 Chaffin, M., et al. (2018), Mars H escape rates derived from MAVEN/IUVS Lyman alpha  
1039 brightness measurements and their dependence on model assumptions, *J. Geophys. Res.*, *123*, p.  
1040 2192–2210, <https://doi.org/10.1029/2018JE005574>

1041 Chamberlain, J. W. (1963), Planetary Coronae and Atmospheric Evaporation, *Planetary & Space*  
1042 *Science*, *8*, p. 901-960.

1043 Chaufray, J. Y., Bertaux, J. L., LeBlanc, F., Quemerais, E. (2008), Observation of the Hydrogen  
1044 Corona with SPICAM on Mars Express, *Icarus*, *195*, 598-613

1045 Chaufray, J. Y., Gonzalez-Galindo, F., Forget, F., Lopez-Valverde, M. A., LeBlanc, F., Modolo,  
1046 R., Hess, S. (2015), Variability of the Hydrogen in the Martian Upper Atmosphere as Simulated  
1047 by a 3D Atmosphere-Exosphere Coupling, *Icarus*, *245*, 282-294.

1048 Chaufray, J.-Y., R. V. Yelle, F. Gonzalez-Galindo, F. Forget, M. Lopez-Valverde, F. Leblanc, R.  
1049 Modolo (2018), Effect of the lateral exospheric transport on the horizontal hydrogen distribution  
1050 near the exobase of Mars, *J. Geophys. Res.: Space Physics*, *123*, p. 2441-2454.

1051 Clarke, J. T., J. Bertaux, J. Y. Chaufray, G. Gladstone, E. Quemerais, J. Wilson, D. Bhattacharyya  
1052 (2014), A Rapid Decrease of the Hydrogen Corona of Mars, *Geophys. Res. Lett.*, *41*, 8013-8020.

1053 Clarke, J. T., *et al.* (2017), Variability of D and H in the martian upper atmosphere observed with  
1054 the MAVEN IUVS echelle channel. *J. Geophys. Res.: Space Physics*, *122*, 2336–2344, doi:  
1055 10.1002/2016JA023479

1056 Clarke, J. (2018), Dust-enhanced water escape, *Nature*, [https://doi.org/10.1038/s41550-018-0383-](https://doi.org/10.1038/s41550-018-0383-6)  
1057 [6](https://doi.org/10.1038/s41550-018-0383-6)

1058 Dostovalev, S. B., and Chuvakhin, S. D. (1973), On the Distribution of Neutral Hydrogen in the  
1059 Upper Atmosphere of Mars, *Cosmic Research*, *11*, 767-773.

1060 Elrod, M. K., S. Bougher, J. Bell, P. R. Mahaffy, M. Benna, S. Stone, R. V. Yelle, B. Jakosky  
1061 (2017), He bulge revealed: He and CO<sub>2</sub> diurnal and seasonal variation in the upper atmosphere of

1062 Mars as detected by MAVEN NGIMS, *J. Geophys. Res.: Space Physics*, 122,  
1063 doi:10.1002/2016JA023482.

1064 Emerich, C., Lemaire, P., Vial, J. C., Curdt, W., Schule, U., Wilhelm, K. (2005), A New Relation  
1065 Between the Central Spectral Solar H I Lyman  $\alpha$  Irradiance and the Line Irradiance Measured by  
1066 SUMER/SOHO During the Cycle 23, *Icarus*, 178, 429-433.

1067 Eparvier, F., P. Chamberlin, T. Woods, E. Thiemann, (2015), The solar extreme ultraviolet monitor  
1068 for MAVEN, *Space Science Reviews*, 195(1-4), 293–301, doi:10.1007/s11214-015-0195-2

1069 Fedorova, A., J. L. Bertaux, D. Betsis, F. Montmessin, O. Korablev, L. Maltagliati, J. Clarke  
1070 (2017), Water vapor in the middle atmosphere of Mars during the 2007 global dust storm, *Icarus*,  
1071 300, p. 440-457.

1072 Forget, F., Hourdin, F., Fournier, R., Hourdin, C., Talagrand, O., Collins, M., Lewis, S. R., et al.  
1073 (1999). Improved general circulation models of the Martian atmosphere from the surface to above  
1074 80 km, *Journal of Geophysical Research*, 104(E10), 24,155–24,175.  
1075

1076 Halekas, J. S. (2017), Seasonal variability of the hydrogen exosphere of Mars, *J. Geophys. Res.*  
1077 *Planets*, 122, doi:10.1002/2017JE005306.

1078 Heavens, N., A. Kleinböhl, M. Chaffin, J. Halekas, D. Kass, P. Hayne, D. McCleese, S. Piqueux, J.  
1079 Shirley, and J. Schofield (2018), Hydrogen escape from Mars enhanced by deep convection in dust  
1080 storms, *Nature*, 2, 126 – 132, doi: 10.1038/s41550-017-0353-4.

1081 Hodges, R. R. Jr., and F. S. Johnson (1968), Lateral transport in planetary atmospheres, *J. Geophys.*  
1082 *Res.*, 73, p. 7307.

1083 Holmström, M (2006), Asymmetries in Mars' Exosphere. Implications for X-ray and ENA  
1084 Imaging, *Space Science Reviews*, 126, p. 435-445.

1085 Hummer, D. G. (1962), Non-coherent scattering, I, The redistribution functions with Doppler  
1086 broadening, *Mon. Not. R. Astron. Soc.*, 125, p. 21-37.

1087 Hunten, D. M., and McElroy, M. B. (1970), Production and Escape of Hydrogen on Mars, *J.*  
1088 *Geophys. Res.*, 75, 5989-6001

1089 Hunten, D. M. (1973), The Escape of Light Gases from Planetary Atmospheres, *J. Atmos. Sci.*, 30,  
1090 1481-1494

- 1091 Hunten, D. M. (1982), Thermal and Non-Thermal Escape Mechanisms for Terrestrial Bodies,  
1092 *Planetary & Space Sciences*, 30, p. 773-783.
- 1093 Krasnopolsky, V. A., Mumma, M. J., Gladstone, G. R. (1998), Detection of Atomic Deuterium in  
1094 the Atmosphere of Mars, *Science*, 280, p. 1576-1580
- 1095 Krasnopolsky, V. A. (2002), Mars' Upper Atmosphere and Ionosphere at Low, Medium and High  
1096 Solar Activities: Implications for Evolution of Water, *J. Geophys. Res.*, 107, 11-1-11-1
- 1097 Lewis, S. R., Collins, M., Read, P. L., Forget, F., Hourdin, F., Fournier, R., Hourdin, C., et al.  
1098 (1999). A climate database for Mars. *Journal of Geophysical Research*, 104(E10), 24,177–24,194.  
1099
- 1100 Mahaffy, P. R., et al. (2015a), The Neutral Gas and Ion Mass Spectrometer on the Mars  
1101 Atmosphere and Volatile Evolution Mission, *Sp. Sci. Rev.*, 195, p. 49-73.
- 1102 Mahaffy, P. R., et al. (2015b), The Imprint of Atmospheric Evolution in the D/H of Hesperian  
1103 Clay Minerals on Mars, *Science*, 347, p. 412-414.
- 1104 Mahaffy, P. R., M. Benna, M. Elrod, R. V. Yelle, S. W. Bougher, S. W. Stone, and B. M. Jakosky  
1105 (2015c), Structure and composition of the neutral upper atmosphere of Mars from the MAVEN  
1106 NGIMS investigation, *Geophys. Res. Lett.*, 42, doi:10.1002/2015GL065329.
- 1107 Matta, M., P. Withers and M. Mendillo (2013), The composition of Mars' topside ionosphere:  
1108 Effects of hydrogen, *J. Geophys. Res.: Space Physics*, 118, p. 2681-2693.
- 1109 Mayyasi, M., et al. (2017a). IUVS echelle-mode observations of interplanetary hydrogen: Standard  
1110 for calibration and reference for cavity variations between Earth and Mars during MAVEN cruise.  
1111 *J. Geophys. Res.: Space Physics*, 122, doi:10.1002/2016JA023466
- 1112 Mayyasi, M., et al. (2017b). The variability of atmospheric deuterium brightness at Mars: Evidence  
1113 for seasonal dependence. *J. Geophys. Res.: Space Physics*, 122, doi:10.1002/2017JA024666
- 1114 Mayyasi, M., Bhattacharyya, D., Clarke, J., Catalano, A., Benna, M., Mahaffy, P., et al. (2018),  
1115 Significant Space Weather Impact on the Escape of Hydrogen from Mars, *Geophys. Res. Lett.*, 45,  
1116 p. 8844-8852, <https://doi.org/10.1029/2018GL077727>.
- 1117 Mayyasi, M., et al. (2019), Seasonal variability of deuterium in the upper atmosphere of Mars, *J.*  
1118 *Geophys. Res.*, doi:10.1029/2018JA026244.

1119 McClintock, W. E., *et al.* (2015), The Imaging Ultraviolet Spectrograph (IUVS) for the MAVEN  
1120 mission, *Sp. Sci. Rev.*, *195*, p. 75-124.

1121 McElroy, M. B., and Donahue T. M. (1972), Stability of the Martian Atmosphere, *Science*, *177*,  
1122 986-988

1123 Nagy, A. F., A. Balogh, T. E. Cravens, M. Mendillo, I. Müller-Wodarg (Eds.) (2009), Comparative  
1124 Aeronomy, ISBN 978-0-387-87824-9.

1125 Parkinson, T. D., and Hunten, D. M. (1972), Spectroscopy and Acronomy of O<sub>2</sub> on Mars, *J. Atmos.*  
1126 *Sci.*, *29*, 1380-1390

1127 Pryor, W., J. Ajello, C. Barth, C. Hord, A. I. Stewart, K. Simmons, W. McClintock, B. Sandel, D.  
1128 Shemansky (1992), The Galileo and Pioneer Venus ultraviolet spectrometer experiments – Solar  
1129 Lyman-alpha latitude variation at solar maximum from interplanetary Lyman-alpha observations,  
1130 *J. Astrophys.*, *394*, p. 363 – 377

1131 Pryor, W.R., G. M. Holsclaw, W. E. McClintock, M. Snow, R. J. Vervack, G. R. Gladstone, S.  
1132 A. Stern, K. D. Retherford, and P. F. Miles (2013), Lyman-alpha models for LRO LAMP based  
1133 on MESSENGER MASCS and SOHO SWAN data, in "Cross-calibration of past and present far  
1134 UV spectra of solar system objects and the heliosphere", ISSI Scientific Report N°13, E.  
1135 Quemerais, M. Snow, R.-M. Bonnet eds., Springer.

1136 Quemerais, E., and Bertaux, J. L. (1993), Radiative Transfer in the Interplanetary Medium at  
1137 Lyman Alpha, *Astron. Astrophys.*, *277*, 283-301.

1138 Rahmati, A. et al. (2017), MAVEN measured oxygen and hydrogen pickup ions: Probing the  
1139 martian exosphere and neutral escape, *J. Geophys. Res.*, *122*, p. 3689-3706.

1140 Rahmati, A. et al. (2018), Seasonal variability of neutral escape from Mars as derived from  
1141 MAVEN pick-up ion observations, *J. Geophys. Res.: Planets*, *123*, p. 1192-1202.

1142 Romanelli, N. et al. (2016), Proton cyclotron waves occurrence rate upstream from Mars observed  
1143 by MAVEN: Associated variability of the martian upper atmosphere, *J. Geophys. Res.*, *121*, p. 11.

1144 Stone, S., R. V. Yelle, M. Benna, M. Elrod, P. Mahaffy (2018), Thermal structure of the Martian  
1145 upper atmosphere from MAVEN NGIMS, *J. Geophys. Res.: Planets*, *123*, p. 2842-2867.

- 1146 Venot, O., Y. Bénilan, N. Fray, M.-C. Gazeau, F. Lefèvre, Et. Es-sebbar, E. Hébrard, M. Schwell,  
1147 C. Bahrini, F. Montmessin, M. Lefèvre, I. P. Waldmann (2018), VUV-absorption cross section of  
1148 carbon dioxide from 150 to 800 K and applications to warm exoplanetary exospheres, *Astron. &*  
1149 *Astrophys.*, 609, id.A34, 13 pp.
- 1150 Vidal-Madjar, A., and J. L. Bertaux (1972), A calculated hydrogen distribution in the exosphere,  
1151 *Planet. & Sp. Sci.*, 20, p. 1147-1162.
- 1152 Villanueva, G., Mumma, M., Novak, R., Käufl, H., Hartogh, P., Encrenaz, T., Tokunaga, A.,  
1153 Khayat, A., Smith, M. (2015), Strong water isotopic anomalies in the martian atmosphere: Probing  
1154 current and ancient reservoirs, *Science*, 348(6231), 218–221, doi:10.1126/science.aaa3630.